Atmospheric
Measurement
Techniques

Evolution under dark conditions of particles from old and modern diesel vehicles in a new environmental chamber characterized with fresh exhaust emissions

Boris Vansevenant[1,2,3], **Cédric Louis**[1,2], **Corinne Ferronato**[3], **Ludovic Fine**[3], **Patrick Tassel**[1], **Pascal Perret**[1], **Evangelia Kostenidou**[4], **Brice Temime-Roussel**[4], **Barbara D'Anna**[4], **Karine Sartelet**[5], **Véronique Cerezo**[1], and **Yao Liu**[1]

[1]EASE, Université Gustave Eiffel, Bron, 69500, France
[2]French Agency for Ecological Transition, ADEME, Angers, 49000, France
[3]IRCELYON, University Claude Bernard Lyon 1, Villeurbanne, 69100, France
[4]LCE, Aix-Marseille University, UMR 7376 CNRS, Marseille, 13331, France
[5]CEREA, Joint Laboratory Ecole des Ponts ParisTech/EdF R&D, University Paris-Est, Marne-la Vallée, 77455, France

Correspondence: Yao Liu (yao.liu@univ-eiffel.fr)

Abstract. Atmospheric particles have several impacts on health and the environment, especially in urban areas. Parts of those particles are not fresh and have undergone atmospheric chemical and physical processes. Due to a lack of representativeness of experimental conditions and experimental artifacts such as particle wall losses in chambers, there are uncertainties on the effects of physical processes (condensation, nucleation and coagulation) and their role in particle evolution from modern vehicles. This study develops a new method to correct wall losses, accounting for size dependence and experiment-to-experiment variations. It is applied to the evolution of fresh diesel exhaust particles to characterize the physical processes which they undergo. The correction method is based on the black carbon decay and a size-dependent coefficient to correct particle distributions. Six diesel passenger cars, Euro 3 to Euro 6, were driven on a chassis dynamometer with Artemis Urban cold start and Artemis Motorway cycles. Exhaust was injected in an $8\,\mathrm{m}^3$ chamber with Teflon walls. The physical evolution of particles was characterized during 6 to 10 h. Increase in particle mass is observed even without photochemical reactions due to the presence of intermediate-volatility organic compounds and semi-volatile organic compounds. These compounds were quantified at emission and induce a particle mass increase up to $17\,\%\,\mathrm{h}^{-1}$, mainly for the older vehicles (Euro 3 and Euro 4). Condensation is 4 times faster when the available particle surface is multiplied by 6.5. If initial particle number concentration is below $[8$–$9]\times 10^4\,\mathrm{cm}^{-3}$, a nucleation mode seems to be present but not measured by a scanning mobility particle sizer (SMPS). The growth of nucleation-mode particles results in an increase in measured [PN]. Above this threshold, particle number concentration decreases due to coagulation, up to $-27\,\%\,\mathrm{h}^{-1}$. Under those conditions, the chamber and experimental setup are well suited to characterizing and quantifying the process of coagulation.

1 Introduction

Air pollution is a major concern due to its impacts on climate, environment and health. It has been classified as carcinogenic to humans by the International Agency for Research on Cancer (IARC, 2016). Its effects are greater in urban areas, where pollutants such as fine particles accumulate and present a serious health risk due to human exposure. Road traffic is an important source of particles in urban environments (Rivas et al., 2020). Many particle-emitting vehicles such as old diesel cars are still present on roads of several countries (average age of road vehicles per country – European Environment Agency, 2020).

Freshly emitted particles and gases undergo physical evolutions in the atmosphere, such as nucleation, coagulation and condensation (Seinfeld and Pandis, 2016). Chemical reactions in the gas phase, enhanced by oxidative processes and photochemistry, form organic compounds with lower volatility (Seinfeld and Pandis, 2016). These compounds can undergo the physical processes of condensation and nucleation, leading to secondary organic aerosols (SOA). SOA are estimated to contribute 50 %–85 % of the organic aerosol (OA) burden (Zhu et al., 2017) and 30 %–77 % of $PM_{2.5}$ during haze pollution in China (Huang et al., 2014). Numerous studies focus on particle evolution and SOA formation in the presence of added oxidants and strong UV lights (Chen et al., 2019; Chu et al., 2016; Lambe et al., 2011; Lu et al., 2019; Sbai et al., 2020; Wang et al., 2018a). They aim at characterizing the photooxidation processes of organic compounds during several hours. This might not be thoroughly representative of all atmospheric conditions (Chen et al., 2019). Several situations exist in which particles evolve with limited light (winter rush hours, nighttime, tunnels), and exposure may occur close to traffic (Harrison et al., 2018) shortly after emissions. In those situations, some physical evolutions took place, but not yet oxidation/photooxidation processes. Some studies focused on physical processes only (Giechaskiel et al., 2005; Harrison et al., 2018; Jeong et al., 2015; Kozawa et al., 2012; Morawska et al., 2008; Zhang et al., 2004; Zhang and Wexler, 2004). They are mainly based on the measurement of particles near freeways or from vehicle exhaust plume. These methods enable the study of emissions under real conditions but are impacted by the presence of external sources and high dilution due to the wind and distant measurement. The presence of external sources (cooking, building, heater, wood burning, biogenic sources, etc.) creates a mixture with the traffic emission. It induces difficulties in evaluating the impact of traffic on atmospheric aerosol. Moreover, few of these studies were conducted in the last decade, resulting in a lack of knowledge on modern vehicles, motorizations and aftertreatment technologies. Some studies focusing on particle physical evolution use a constant volume sampler (CVS) (Louis et al., 2017), but they are limited by the short residence time.

Moreover, the physical processes of condensation and nucleation depend in part on concentrations of gas-phase particle precursors, such as semi-volatile and intermediate-volatility organic compounds (SVOCs and IVOCs, respectively). IVOCs can participate in physical evolutions and SOA formation (Sartelet et al., 2018; Xu et al., 2020), but their quantification is impacted by sampling methodology. The uncertainties arise from the effects that dilution and temperature have on the gas-particle partitioning. They also come from the chemical identification to quantify total IVOCs (Xu et al., 2020; Zhao et al., 2016, 2015). This results in a lack of knowledge on their emissions and on the effect of motorization and aftertreatment technologies (Drozd et al., 2019; Zhao et al., 2015). This also impacts the understanding of their role in particle evolutions and the accuracy of atmospheric models (Sartelet et al., 2018; Zhao et al., 2018). More investigations should consequently be conducted to characterize the IVOC and SVOC emissions from modern vehicles equipped with different aftertreatment technologies. The particle physical evolutions during several hours and under controlled experimental conditions should also be investigated. The studies focusing only on vehicle emissions are complementary to those performed near freeways with the presence of other sources and with photochemistry. This would help better understand the actual contribution of road traffic to particle pollution.

Laboratory studies on particle evolutions are often performed in atmospheric chambers. They are a good means of investigating the physical processes of nucleation, condensation and coagulation. The study of those processes requires information on particle concentrations, sizes and distributions (Leskinen et al., 2015; Nah et al., 2017; Pierce et al., 2008; Wang et al., 2018b). However, these parameters are affected by leakage and wall deposition due to Brownian diffusion, gravitational settling, turbulence and electrostatic charge of the Teflon walls (Leskinen et al., 2015; Nah et al., 2017; Pierce et al., 2008; Seinfeld and Pandis, 2016; Wang et al., 2018b, 2014). Leakage and wall deposition of particles induce a decrease in particle mass over time. This prevents the analysis of the mass evolutions from condensation or evaporation of organic material onto or from pre-existing particles. Moreover, since wall deposition depends on particle diameter, it affects the distribution evolutions and therefore the ability to quantify the role of coagulation. It also affects the observation of nucleation-mode particles. Particle data in chambers therefore need to be corrected for leakage and wall losses.

Some studies (Grieshop et al., 2009; Nah et al., 2017; Pathak et al., 2007) have used size-independent wall loss correction methods. This is usually done with the help of a tracer, such as black carbon, assumed to be reliable and enabling the consideration of the experiment-to-experiment variations. However, particle wall losses are known to be size-dependent (Charan et al., 2018; La et al., 2016; Leskinen et al., 2015; Pierce et al., 2008; Wang et al., 2018b; Weitkamp et al., 2007). The use of the same correction coefficient for the whole distribution can mislead the observation of processes such as coagulation. Other studies have therefore used size-dependent correction methods (Nah et al., 2017; Pierce et al., 2008; Wang et al., 2018b). They enable a more precise analysis of the processes affecting the size distribution. However, those methods are usually based on the decay of ammonium sulfate particles (Wang et al., 2018b). They assume that their loss rates are the same as those of the studied particles. Furthermore, the loss rate studies cannot be conducted simultaneously with the actual experiments. They are therefore usually carried out before and after the campaign, thus preventing the experiment-to-experiment variations from being accounted for (Wang et al., 2018b).

Firstly, this study presents the characterization of a new $8\,m^3$ cubic chamber with Teflon walls, aimed at studying the physical particle evolutions from a wide range of on-road vehicles. Six diesel vehicles (two without diesel particle filter (DPF) Euro 3 and Euro 4; three Euro 5 with additive DPF or catalyzed DPF; one Euro 6 with additive DPF and a selective catalytic reducer – SCR) were tested to develop the new leakage and size-dependent wall loss correction method. Five gasoline vehicles (three with port fuel injection Euro 3, 4 and 5; two Euro 5 with direct injection) were also used. The new leakage and wall loss correction method is based on the complementarity of a tracer (black carbon) and a size-dependent equation to correct wall losses. It accounts for experiment-to-experiment variations.

Secondly, this study presents the emissions and evolutions of particles from the six diesel vehicles, Euro 3 to Euro 6, under urban and motorway conditions. Emission factors (EFs) of particle number (PN), particle mass (PM), black carbon (BC), non-methane hydrocarbons (NMHCs) and IVOCs are estimated. They are used to discuss the impact of aftertreatment technologies on emissions and particle evolutions. Moreover, the results of the diesel particle physical evolutions in the chamber under dark conditions are presented. Data are corrected for leakage and wall losses using the new correction method. The physical processes are characterized in the dark in order to better understand their share in particle evolution mechanisms. This study is complementary to those focusing on photochemical processes to better evaluate the total contribution of road traffic to atmospheric particle pollution.

2 Methods

2.1 Chassis dynamometer

The vehicles are tested on a chassis dynamometer used to reproduce different driving conditions. The two non-power wheels are fixed to the floor, while the two power wheels are placed on a rotating $48''$ (121.92 cm) roller. The speed can go up to $200\,km\,h^{-1}$ and is given by the driving guide in front of the vehicle. The dynamometer can apply traction or resistance to the wheels to reproduce the effects of inertia, vehicle load, slope, rolling resistance and aerodynamic resistance. A ventilation system is placed in front of the vehicle to avoid overheating of the engine. The air is blown with a flow proportional to the vehicle speed to cool the engine similarly to how it would be on the road.

2.2 Artemis cycles

The vehicles are tested with the Artemis Urban cold start (UC) cycle and the Artemis Motorway (MW) cycle (André, 2004). They represent specific driving conditions, typical of urban environments and highways, and are chosen to simulate emissions found within big cities (small streets and ur-

ban highways). The speed profiles are given in Fig. A1 for the UC cycle and the MW cycle.

2.3 Vehicles

Dynamometer tests are performed with diesel and gasoline passenger cars (PCs) whose characteristics are given in Table 1. Six diesel vehicles are used in this study: two vehicles without DPF, Euro 3 (D1) and Euro 4 (D2); three Euro 5 vehicles, two with additive DPFs (D3 and D4) and one with a catalyzed DPF (D5); one Euro 6 vehicle (D6) equipped with an additive DPF and a SCR. Five gasoline vehicles are tested: three with port fuel injection (PFI), G1 to G3 with standards Euro 3, 4 and 5; two Euro 5 vehicles with direct injection (DI), G4 and G5.

2.4 Exhaust gas sampling and injection into the chamber

Exhaust gas is sampled from the tailpipe by an ejector dilutor (Dekati L7, Sapelem $50\,NL\,min^{-1}$, Sapelem $1\,NL\,min^{-1}$). The dilutor works with air which is dehumidified, filtered using HEPA particle filters and activated carbon, and heated at $120°$ using a Fine Particle Sampler (FPS; Dekati, 4000). Exhaust gas is diluted between 3 and 20 times, depending on air pressure and ejector dilutor type. The air and exhaust gas are injected into the chamber at a height of 90 cm through a 2 to 4 m-long stainless-steel line. The line is heated at $120\,°C$ to avoid condensation and deposition on its inner surface. The heated line is cleaned after each injection with hot dry clean air during a couple of hours.

2.5 Environmental chamber

The study of the exhaust particle evolution is performed inside the Université Gustave Eiffel (UGE) $8\,m^3$ cubic chamber. The structure of the chamber is made of aluminum, and the walls are made with a $70\,\mu m$-thin Teflon film, used because chemically inert. However, it can be electrostatically charged and influence the wall deposition of gas and particles inside the chamber. The theoretical total volume is $8000\,L$, but it can vary ($\pm 300\,L$) due to deformation of the walls, depending on inner pressure. To avoid contamination from the outside, the chamber is always kept at a slight overpressure ($\sim 5\,Pa$) by injection of clean air. This also compensates for the losses by leakage and instrument sampling. This injection induces dilution inside the chamber. The temperature, humidity and relative pressure are continuously monitored. Instruments sample the air of the chamber at the center at five different heights: 20, 60, 100, 140 and 180 cm.

2.6 Cleaning

Before the first experiment, the inner walls of the chamber were cleaned by hand with microfiber cloth. While this removes most particles and gaseous species on the walls, it also

Table 1. Characteristics of the diesel and gasoline vehicles used in this study for the chamber characterization and the particle evolution.

Diesel vehicles						
Vehicle	D1	D2	D3 (add DPF)	D4 (add DPF)	D5 (cat DPF)	D6 (add DPF and SCR)
Standard	Euro 3	Euro 4	Euro 5	Euro 5	Euro 5	Euro 6
Mass (kg)	1290	1085	1080	1515	1200	1090
Mileage (km)	191 612	95 982	105 823	103 000	85 617	43 919
Aftertreatment technologies	DOC[1]	DOC	DOC + add DPF[2]	DOC + add DPF	DOC + cat DPF	DOC + SCR[3] + add DPF

Gasoline vehicles					
Vehicle	G1 (PFI)	G2 (PFI)	G3 (PFI)	G4 (DI)	G5 (DI)
Injection	PFI[4]	PFI	PFI	DI[5]	DI
Standard	Euro 3	Euro 4	Euro 5	Euro 5	Euro 5
Mass (kg)	1185	1170	1030	1100	1285
Mileage (km)	195 305	95 096	27 712	97 089	92 550
Aftertreatment technologies	TWC[6]	TWC	TWC	TWC	TWC

[1] DOC: diesel oxidation catalyst, [2] DPF: diesel particle filter, [3] SCR: selective catalyst reducer, [4] PFI: port fuel injection, [5] DI: direct injection, [6] TWC: three-way catalyst.

induces high electrostatic charge due to friction of the cloth on Teflon. Manual cleaning was therefore only done once. At the end of each experiment, cleaning is performed with injection of dry clean air, with flow rates varying between 150 and 300 L min^{-1}. Cleaning lasts a minimum of 12 h, thus renewing the air inside the chamber at least 13 times. Since dilution induces an exponential decrease in the pollutant concentrations, this gives a minimum theoretical percentage of clean air inside the chamber of 99 %.

2.7 Instruments

2.7.1 Gas-phase analysis

Non-methane hydrocarbons (NMHCs) are measured either directly from the tailpipe with a Horiba Portable Emissions Measurement System (PEMS) or after a CVS by flame ionization detection with a Horiba analysis system.

IVOCs are collected from the heated line (prior injection into the chamber) by sampling diluted exhaust through stainless-steel tubes filled with Tenax TA at a flow rate of 45 mL min^{-1}. The samples are collected during the entire driving cycle. Collected samples are further analyzed by automatic thermal desorption coupled with a gas chromatography-mass spectrometry detector (ATD-GC-MS). The Markes Unity thermodesorber and a GC6890 gas chromatograph from Agilent fitted with the MS5973 mass spectrometer from Agilent are used. The thermal desorption system consists of a two-stage desorption. During the first desorption step, the compounds are desorbed by heating the Tenax TA under a stream of helium and are condensed on a trap filled with adsorbent and maintained at $-5\,°C$. Dur-

ing the second desorption, the second trap is flash-heated to 300 °C for a rapid introduction of the compounds into the chromatographic column. The chromatographic column used is an Agilent HP1MS 30 m × 0.25 mm, 0.25 µm. The mass spectrometer operates in scanning mode at an electron ionization of 70 eV. Mass spectral data are acquired over a mass range of 33–450 amu. Qualitative identification of compounds is based on the match of the retention time and confirmed by matching their mass spectra with those of standards and from the NIST mass spectral library. Quantification is conducted by the external standard method. Known amounts (1 µL) of standard solutions of volatile organic compounds (VOCs) and IVOCs are introduced into cleaned Tenax TA tubes using an automatic heated GC injector. The calibration tubes are analyzed under the same conditions as mentioned before. The chromatogram shows an unresolved complex mixture, mainly composed of co-eluted hydrocarbons which cannot be further separated by single-dimensional GC. The alkanes (linear and branched) are quantified by an SIR-based response factor of these compounds using the fragment of $m/z = 57$. The response factor used for quantification of branched alkanes is the one of the compounds with the same number of carbon as its parent chain. The fragment $m/z = 83$ is used for the quantification of cyclohexane and of the other cyclic compounds. The fragment $m/z = 78$ is used for the quantification of benzene and $m/z = 91$ for other aromatics. The fragment $m/z = 128$ is used for the quantification of naphthalene. The compounds from the standard solutions taken for quantification of each identified compound are listed in Table 2. The use of response factors from different compounds than the identified ones can induce some error in their quantification. Over the

Table 2. List of the compounds from the standard solutions whose response factors were chosen for quantification of the identified compounds for vehicles D1, D4 and D5 as well as vehicles D2, D3 and D6. The identified alkanes are sorted by the number of carbon atoms in their parent chain: C_{12} to C_{16}, C_{17} to C_{20} and $C_{>20}$.

Identified compounds	Compounds from standard solutions whose response factors were taken for quantification	
	Vehicles D1 and D5	Vehicles D2, D3 and D6
n-alkanes C_{12} to C_{16} b-alkanes with parent chains C_{12} to C_{16}	Dodecane Tridecane Tetradecane Pentadecane Hexadecane	Dodecane Tridecane Tetradecane Pentadecane Hexadecane
n-alkanes C_{17} to C_{20} b-alkanes with parent chains C_{17} to C_{20}	Heptadecane Octadecane Nonadecane Eicosane	hexadecane
n-alkanes $C_{>20}$ b-alkanes with parent chains $C_{>20}$	Eicosane	Hexadecane
Naphthalene	Naphthalene	Toluene
Cycloalkanes in the IVOC retention time range	Cyclohexane	R-cyclohexane
Aromatics in the IVOC retention time range with $C_{\leq 9}$	Branched benzene (C_9)	Branched benzene (C_9)
Aromatics in the IVOC retention time range with $C_{\geq 10}$	Branched benzene (C_{10})	Branched benzene (C_{10})

whole range of IVOCs, this error is estimated to be below 8 % (7.8 % and 0.4 %, respectively, for two urban cycles). For single SVOCs, the errors range from 90 % to 98 %. Since all compounds above C_{22} are quantified using compounds with different carbon numbers (C_{20} for vehicles D1 and D5 and C_{16} for vehicles D2, D3, and D6), the impact on their quantification is important. They are however on the same order for all vehicles and allow comparison between vehicles and driving conditions.

Linear (n-) and branched (b-)alkanes are classified according to their number of carbon C as an indicator of their effective saturation concentration according to Zhao et al. (2015). Alkanes with $C_{<12}$ are considered to be VOCs, alkanes from C_{12} to C_{22} are considered to be IVOCs, and alkanes with $C_{>22}$ are considered to be SVOCs. Also according to Zhao et al. (2015), IVOCs are considered to be the sum of n- and b-alkanes (from C_{12} to C_{22}), naphthalene, as well as aromatics and cycloalkanes in the same retention time bin as C_{12}–C_{22} alkanes.

The CO_2 concentration is measured from the chamber using a MIR2M (Environment SA), which samples air at $1.5\,L\,min^{-1}$. The temporal resolution is 1 s, and the analytical uncertainty is 0.001 %.

2.7.2 Particle-phase analysis

Particle concentrations and size distributions are measured with a scanning mobility particle sizer (SMPS, TSI) composed of an advanced aerosol neutralizer (3087), a differential mobility analyzer (DMA, 3081) column, and a condensation particle counter (CPC, 3775). The sampling flow is $0.3\,L\,min^{-1}$. Classification is based on the particle electrical mobility, and the measurement range goes from 14 to 615 nm. The particle mass is computed, with the assumption that particles are spherical, with an arbitrary density of 1.2 (Barone et al., 2011; Totton et al., 2010). Data are given with a 5 min timescale, with a 5 % analytic uncertainty.

The black carbon concentration is measured using an AE33-7 aethalometer from Magee Scientific. Air is sampled at $2\,L\,min^{-1}$ on filter tape. The black carbon concentration is given by absorption measurements at 880 nm (Andreae and Gelencser, 2006). Data are given with a timescale of 1 min.

2.8 Ammonium sulfate experiments

In order to test the wall losses correction method with nonvolatile inert seeds, experiments are performed with ammonium sulfate particles. Particles are generated from diluted solutions using an atomizer aerosol generator (TSI, 3079A) at a flow rate of $5\,L\,min^{-1}$ during 20 min to 2.5 h. After injec-

Table 3. Characteristics of the ammonium sulfate experiments.

Concentration of solution (mg L^{-1})	Injection duration (min)	Initial [PN][1] (cm^{-3})	Initial [PM][2] (cm^{-3})	Initial mode (nm)
25.0	33	5589	0.5	40.0
50.0	60	8100	0.9	40.0
10.0	24	19 197	2.3	41.4
50.0	120	37 931	7.2	59.4
10.0	167	50 622	17.2	68.5

[1] [PN]: particle number concentration, [2] [PM]: particle mass concentration.

tions, particles reached concentrations ranging from 5500 to 50 600 cm^{-3}. Characteristics of these experiments are given in Table 3.

2.9 Summary of the experiments

Table 4 summarizes the experimental conditions for the six diesel and five gasoline vehicles. Most experiments are performed under similar conditions and are repeated at least twice. For the D4 and G3 vehicles, different conditions are tested. The line was heated once at 80 °C instead of 120 °C, showing no specific influence on particle concentration in the chamber. Also, different ejector dilutions are tested and show a great impact on the initial particle concentrations in the chamber. An ideal dilution of 8.4 is found, leading to total dilution in the chamber between 65 and 130. It is considered ideal for the sake of this study since it enables us to have diluted exhaust giving particle concentrations covering a wide range, depending on emissions. This variety in initial particle concentration is important to study the influence of initial concentration on particle evolution.

2.10 Chamber characterization

2.10.1 Mixing time

During injection inside the chamber, turbulence is induced due to the flow of exhaust gas, and the mixture is not homogeneous right after the end of injection. Moreover, to avoid the increase in particle deposition surface and turbulence (Crump et al., 1982; Nomura et al., 1997), there is no fan system to make the mixture homogeneous. To determine the necessary time to have a homogeneous mixture inside the chamber, CO_2 is injected, and the concentration is measured at three of the five sampling heights of the chamber: the bottom one (20 cm), the middle one (100 cm) and the top one (180 cm). The average concentration over the five sampling heights is also monitored during injection of CO_2.

2.10.2 Leakage

Leakage describes the loss of pollutants and air due to over-pressure through the corners and door of the chamber. The leak rate is quantified experimentally using two complementary methods. The first method, called the "pressure method", uses injection of air inside the chamber. A constant flow of air is injected at a precise value. Simultaneously, pressure is monitored, and when it becomes stable, it means that the flow or air exiting the chamber (e.g., leak flow) is the same as the one injected. This experiment is realized with different flow rates from 0.1 up to 6.0 L min^{-1}.

The second method uses measurement of the CO_2 concentration and is referred to as the "CO_2 method". High concentrations of CO_2 are injected inside the chamber, and the concentration decay is observed at constant pressure. This method was used by Papapostolou et al. (2011) with the CO decay. The CO_2 concentration decreases exponentially due to dilution by compensation of air injected into the chamber and to leakage at a given relative pressure varying between 0.17 and 18.42 Pa. The decay coefficient is converted into a leak flow, expressed in L min^{-1}, thus allowing comparison with the "pressure-method" results. The leak flow (F_{leak}) can also be expressed as a leak rate (Rate$_{leak}$), given as the percentage of the total volume exiting the chamber in 1 h, according to Eq. (1).

$$\text{Rate}_{\text{leak}} \left(\% \, \text{vol} \, \text{h}^{-1} \right) = \frac{100 \times 60 \times F_{\text{leak}}}{8000} \tag{1}$$

2.10.3 Wall losses

The leakage and size-dependent wall loss correction method presented in this study is based on four consecutive steps. Step 1 consists in correcting total [PM] using the decay of the black carbon concentration [BC]. During step 2, the particle distribution is corrected using a size-dependent wall loss coefficient. This coefficient is based on the theory of Crump and Seinfeld (1981), with an arbitrary estimation of the turbulence. Step 3 consists in optimizing the turbulence parameter k_e to fit corrected data with results of step 1. Finally, step 4 is the computation of the total particle number and mass-corrected concentrations.

– Step 1. [PM] correction using [BC]

The first step consists in correcting the total particle mass, using BC as a tracer for primary particle emissions, as done by Grieshop et al. (2009). As BC is an inert compound (Platt et al., 2013; Wang et al., 2018b), the decay of its concentration is due to leakage and wall deposition, with a loss rate k_{BC}. Another tracer could be used as long as it represents total particle losses. By assuming that particles are internally mixed, total particle mass has the same loss rate as BC (Grieshop et al., 2009; Hennigan et al., 2011; Platt et al., 2013). This assumption can induce some uncertainty if the loss rate is

Table 4. Summary of the conditions for the diesel and gasoline experiments.

Vehicle	Standard	Line temp. (°C)	Ejector dilution	Artemis Urban cold start		Artemis Motorway	
				Number of cycles	Total dilution	Number of cycles	Total dilution
Diesel vehicles							
D1	Euro 3	120	8.4	2	97	3	65
D2	Euro 4	120	8.4	2	97	3	130
D3 (add DPF)	Euro 5	120	8.4	2	97	2	65–130
D4 (add DPF)	Euro 5	80–120	2.3–15.0	2	19–387	1	26
D5 (cat DPF)	Euro 5	120	8.4	2	97	2	65
D6 (add DPF and SCR)	Euro 6	120	8.4	1	97	1	65
Gasoline vehicles							
G1 (PFI)	Euro 3	120	8.4	1	97	3	65
G2 (PFI)	Euro 4	120	8.4			1	130
G3 (PFI)	Euro 5	120	2.3–8.4	3	19	4	13–130
G4 (DI)	Euro 5	120	8.4	2	97	2	130
G5 (DI)	Euro 5	120	8.4	2	97	1	130

size-dependent (Wang et al., 2018b). Still, it appears to be a good estimation of the [PM] losses due to leakage and wall losses and has been used in several chamber studies (Grieshop et al., 2009; Hennigan et al., 2011; Platt et al., 2013). A corrected PM concentration can thus be obtained at all times of each experiment with Eq. (2).

$$[PM]^{\text{step 1}}_{\text{corrected}}(t) = [PM]_{\text{measured}}(t) \times \exp(k_{\text{BC}} \times t) \quad (2)$$

For some experiments, the decay of [BC] cannot accurately be fitted by a first-order exponential decay. In those cases, the term $\exp(k_{\text{BC}}t)$ is replaced by $[BC]_{t0} / [BC]_t$. This has no consequences for the corrected [PM], since the term $\exp(k_{\text{BC}} \times t)$ in Eq. (2) is equal to $[BC]_{t0} / [BC]_t$ assuming a first-order exponential decay. Both corrections are therefore equivalent, the only goal being to simulate the [BC] evolution as well as possible.

This corrected concentration $[PM]^{\text{step 1}}_{\text{corrected}}(t)$ represents the evolution of particle mass due to nucleation or condensation/evaporation of organic material. Particles lost to the walls are assumed to be at equilibrium with suspended ones (Grieshop et al., 2009).

– Step 2. Particle-size-dependent correction

The second step consists in correcting particle mass and number concentration, accounting for the size dependence of wall deposition (Charan et al., 2018; Leskinen et al., 2015; Pierce et al., 2008; Wang et al., 2018a, b). The aerosol wall deposition rate due to turbulent diffusion, Brownian diffusion and gravitational sedimentation is given in Eq. (3) (Corner and Pendlebury, 1951;

Crump and Seinfeld, 1981). It is given for a cubic chamber of side length L, as a function of particle diameter D_{p}.

$$\beta_i(D_{\text{p}}) = \frac{1}{L} \times \left[\frac{8\sqrt{k_{\text{e}}D(D_{\text{p}})}}{\pi} + v(D_{\text{p}}) \times \coth\left(\frac{\pi v(D_{\text{p}})}{4\sqrt{k_{\text{e}}D(D_{\text{p}})}}\right) \right], \quad (3)$$

with i the SMPS particle size channel of geometric midpoint diameter D_{p}, k_{e} the eddy diffusivity coefficient (s^{-1}), $D(D_{\text{p}}) = \frac{k_{\text{boltz}}TC_{\text{c}}}{3\pi\mu D_{\text{p}}}$ the Brownian diffusivity (m^2 s^{-1}), $v(D_{\text{p}}) = \frac{D_{\text{p}}^2\rho_{\text{p}}gC_{\text{c}}}{18\mu}$ the terminal particle velocity (m s^{-1}), and C_{c} the Cunningham slip-correction factor $C_{\text{c}} = 1 + \frac{2\lambda}{D_{\text{p}}} \times \left[1.257 + 0.4 \times \exp\left(-\frac{1.1 \times D_{\text{p}}}{2\lambda}\right)\right]$.

All terms of this equation, except for k_{e}, can be found using literature (Crump and Seinfeld, 1981; Seinfeld and Pandis, 2016) and experimental data. They are listed in Appendix B. The k_{e} coefficient represents the turbulence inside the chamber, induced by the exhaust gas injection, the air flow to compensate leakage and sampling, and electrostatic forces near the walls (Charan et al., 2018; Crump and Seinfeld, 1981; Pierce et al., 2008; Seinfeld and Pandis, 2016; Wang et al., 2018b). As it cannot be measured (Charan et al., 2018), k_{e} will in a first instance be given an arbitrary value in order to compute $\beta_i(D_{\text{p}})$. The rate of leakage is taken as defined by Schnell et al. (2006) as the ratio of the flows entering (or exiting) the chamber $\dot{V}$ by the volume of

the chamber V: $\alpha = \dot{V}/V$. It follows a similar basis to the "pressure method" defined above. It assumes that at constant pressure, the flow of air injected into the chamber is equal to the sum of leakage and of what is sampled by the instruments. It is determined for each experiment using the flow of air injected into the chamber $\dot{V}$ ($\mathrm{L\,s^{-1}}$) and the total volume of the chamber V. The loss of particles due to leakage and wall deposition in each size bin can then be estimated for the arbitrary value of k_e. Assuming that the coefficients α and β_i (D_p) are constant over the course of each experiment, the loss process is a first-order exponential decay (Leskinen et al., 2015; Nah et al., 2017; Pierce et al., 2008; Verheggen and Mozurkewich, 2006; Wang et al., 2018b, a, 2014) given by Eq. (4).

$$\left. [PM_i]_{\text{lost}}^{\text{step 2}}(t)\right|_{\text{arbitrary}\,k_e} = [PM_i]_{\text{measured}}(t)$$
$$\times \left(1 - e^{-(\alpha+\beta_i)\times t}\right) \quad (4)$$

By adding this to the measured distribution at time t ($[PM_i]_{\text{measured}}(t)$), a distribution corrected for leakage and wall deposition can be obtained. It represents the particle mass distribution evolution solely due to photochemical and physical processes (Eq. 5).

$$\left. [PM_i]_{\text{corrected}}^{\text{step 2}}(t)\right|_{\text{arbitrary}\,k_e} = [PM_i]_{\text{measured}}(t)$$
$$+ [PM_i]_{\text{lost}}^{\text{step 2}}(t) \quad (5)$$

The corresponding total mass concentration can be computed with Eq. (6). The factor 64 comes from the fact that multiple charge corrections are based on a 64-channel resolution (TSI, 2010).

$$\left. [PM]_{\text{corrected}}^{\text{step 2}}(t)\right|_{\text{arbitrary}\,k_e} =$$
$$\frac{\sum \left. [PM_i]_{\text{corrected}}^{\text{step 2}}(t)\right|_{\text{arbitrary}\,k_e}}{64} \quad (6)$$

– Step 3. Optimization using a least-squares error algorithm

So far, the evolution of the total particle mass corrected for leakage and wall deposition has two different expressions. They both represent the evolution of total particle mass in the chamber solely due to photochemical and physical processes of nucleation and condensation (coagulation can also occur but has no effect on particle mass). However, the expression obtained during step 2 $\left(\left. [PM]_{\text{corrected}}^{\text{step 2}}(t)\right|_{\text{arbitrary}\,k_e}\right)$ is attached to high uncertainties as it is found for an arbitrary value of k_e. Charan et al. (2018) realized an optimal fitting of experimental data to determine the parameter k_e. Following the same

idea, an optimization of k_e is performed to minimize the difference between the corrected PM concentrations obtained during step 1 (considered to be the reference) and during step 2 (Eq. 7).

$$\sum_{t=t_0}^{t=t_{\text{final}}} \left\{ [PM]_{\text{corrected}}^{\text{step 1}}(t) - \left. [PM]_{\text{corrected}}^{\text{step 2}}(t)\right|_{\text{optimized}\,k_e} \right\}^2$$
$$\xrightarrow{k_e} \text{minimum} \quad (7)$$

This operation results in an optimized expression of β_i (D_p) for each chamber experiment. It is used in the equations of step 2 (Eqs. 3, 4, 5 and 6) to obtain corrected distributions and total concentrations. The values of β_i (D_p) are used to compute a mean wall loss coefficient $\beta_{k_e}^{\text{mean}}$, depending on the k_e value found after optimization. To account for the SMPS bins, each β_i (D_p) is weighted with the relative size of the channel i (D_p), according to Eq. (8).

$$\beta_{k_e}^{\text{mean}} = \sum_{D_{p,\text{min}}}^{D_{p,\text{max}}} \left[\beta_i\left(D_p\right) \times \frac{D_{p,i+1} - D_{p,i}}{D_{p,\text{max}+1} - D_{p,\text{min}}} \right], \quad (8)$$

with $D_{p,i}$ the diameter associated with the bin i, with D_p ranging from 14.1 to 615.3 nm, $D_{p,i+1} - D_{p,i}$ the size of the bin i, where $D_{p,\text{max}+1} = 637.8$ nm, and $\sum(D_{p,i+1} - D_{p,i}) = 623.7$ nm the total measurement range considered in this study.

$\beta_{k_e}^{\text{mean}}$ represents the average wall loss coefficient for all particle diameters in the distribution. Combined with the leakage coefficient α, it leads to an optimized coefficient $\alpha + \beta_{k_e}^{\text{mean}}$ representing the rate of total particle losses due to leakage and size-dependent wall deposition. This coefficient is never actually applied: it is an average of the coefficients $\alpha + \beta_i$ (D_p) which are applied to each particle size bin. Also, $\alpha + \beta_{k_e}^{\text{mean}}$ can be compared to k_{BC} to make sure that it accurately describes total losses.

– Step 4. Corrected number distribution and number concentration

The size-dependent optimized loss coefficient $\alpha + \beta_i$ (D_p), from which $\alpha + \beta_{k_e}^{\text{mean}}$ is computed, can be applied to the number distribution to determine what is lost due to leakage and wall deposition (Eq. 9).

$$[PN_i]_{\text{lost}}(t) = [PN_i]_{\text{measured}}(t_0) \times \left(1 - e^{-(\alpha+\beta_i)\times t}\right) \quad (9)$$

This lost distribution can be added to the measured one to obtain a corrected number distribution (Eq. 10). The corresponding corrected total number concentration can be computed (TSI, 2010) with Eq. (11). This method enables us to correct the concentration variations in a size bin which are due to leakage and wall deposition.

The remaining variations are due to physical processes only and can therefore be analyzed.

$$[PN_i]_{\text{corrected}}(t) = [PN_i]_{\text{measured}}(t) + [PN_i]_{\text{lost}}(t) \quad (10)$$

$$[PN]_{\text{corrected}}(t) = \frac{\sum [PN_i]_{\text{corrected}}(t)}{64} \quad (11)$$

This method can also be used to determine the size-dependent loss rate β_i (D_p) for seed-only experiments with ammonium sulfate particles. The evolution of those particles is not impacted by effects of condensation or evaporation. This means that the corrected total mass of ammonium sulfate particles should be a constant, equal to the concentration at time t_0, as expressed in Eq. (12). This corrected mass is used as the reference in Eq. (7) of step 3. The mass concentration decay is associated with a rate $k_{\text{PM}}^{\text{amm sul}}$, which represents the losses due to leakage and wall deposition only. It can therefore be compared to the rate k_{BC} found for exhaust particle experiments.

$$[PM]_{\text{corrected}}^{\text{step 1}}(t) = [PM]_{\text{measured}}^{\text{seed only}}(t_0) \quad (12)$$

3 Results

3.1 Chamber characterization

3.1.1 Mixing time

Mixing time is investigated using CO_2 measurements at three sampling heights as presented in Fig. 1a. They show that just 1 min after the end of the CO_2 injection, the vertical gradient of CO_2 is important. The mean CO_2 concentration is $0.977 \pm 0.013\%$, but this value reaches 0.964% at the top of the chamber and 0.990% at the bottom. After 20 min, the mean concentration is $0.972 \pm 0.003\%$, with a minimum value of 0.969% at the top and 0.975% at the bottom. From that time, the concentration variability is less than 1% between the minimum and maximum values, and the mixture can be considered homogeneous. After 1 h, the mixture is homogeneous if the instrument uncertainties are accounted for.

The CO_2 concentration averaged over the five sampling heights is shown in Fig. 1b. Results show that the mean concentration increases rapidly during the first 20 min following injection. Then it reaches its maximum and remains stable. At this stage, the mixture can be considered homogeneous.

The results of the CO_2 tests indicate that the mixture inside the chamber can be considered homogeneous 20 min after the end of injection. Therefore, in this study, all the chamber analyses will start 20 min after the end of the exhaust gas injection.

3.1.2 Leakage

The leak flows obtained with the "pressure method" and the "CO_2 method" are presented in Fig. 2 with the green and black curves, respectively.

Both methods give similar results. A numerical fit of the curves gives a mathematical expression (Eq. 13) for the leak flow F_{leak} (L min^{-1}) as a function of the relative pressure ΔP (Pa) between the chamber and outside.

$$F_{\text{leak}}\left(\text{L min}^{-1}\right) = (1.13 \pm 0.12) \times \Delta P^{0.59 \pm 0.04} \quad (13)$$

For values of relative pressure between 0.2 and 5 Pa, the leak flow is between 0.4 and $2.9\,\text{L min}^{-1}$, corresponding to a leak rate between $0.3\,\%\,\text{vol h}^{-1}$ and $2.2\,\%\,\text{vol h}^{-1}$. Platt et al. (2013) reported for the Paul Scherrer Institute (PSI) chamber an average leak rate of $0.08\,\%\,\text{vol h}^{-1}$. This is lower than the one found in this study, probably due to the fact that the chamber is operated under overpressure conditions. This leak rate can be used to estimate gas- and particle-phase leakage from the measured relative pressure. For this study, a leak rate is estimated for each experiment, without the dependency on the relative pressure. Indeed, it can change between the end of injection and the rest of the chamber experiment (the leakage due to high overpressure measured right after injection is not accounted for but decreases rapidly). Another leak definition is given in the wall losses section, with a similar basis to the "pressure method" and taking into account the instrument sampling flows.

3.1.3 Wall losses

The four-step correction method is applied to more than 50 experiments using particles from passenger car exhausts (diesel or gasoline) and ammonium sulfate particles. The associated experimental protocols are described in the Methods part. The optimization processes give k_e values between 0.001 and $27.32\,\text{s}^{-1}$, with an average of $2.41\,\text{s}^{-1}$. The corresponding wall loss coefficients are, respectively, 1.05×10^{-4}, 1.58×10^{-2} and $4.69 \times 10^{-3}\,\text{min}^{-1}$ for a particle of diameter 100 nm. These values are similar to those reported by Leskinen et al. (2015) and Babar et al. (2017), of 7.50×10^{-4} and $3.96 \times 10^{-3}\,\text{min}^{-1}$, respectively. Figure 3 shows the size distribution of the wall loss coefficient β_i (D_p) as well as the corresponding mean wall loss coefficient $\beta_{k_e}^{\text{mean}}$ for three values of k_e in this range: $k_e = 0.36\,\text{s}^{-1}$; $k_e = 2.57\,\text{s}^{-1}$; $k_e = 16.70\,\text{s}^{-1}$. These values are chosen to represent the lower part of the range, the average, and the upper part of the range, respectively. The mean wall loss coefficients are, respectively, 1.31×10^{-3}, 8.44×10^{-3}, and $2.13 \times 10^{-2}\,\text{min}^{-1}$.

Figure 3 shows that for a given k_e, wall losses vary greatly as a function of the particle diameter in the range 15–600 nm. They are higher for smaller particles due to higher Brownian diffusion. These results also show that the wall loss
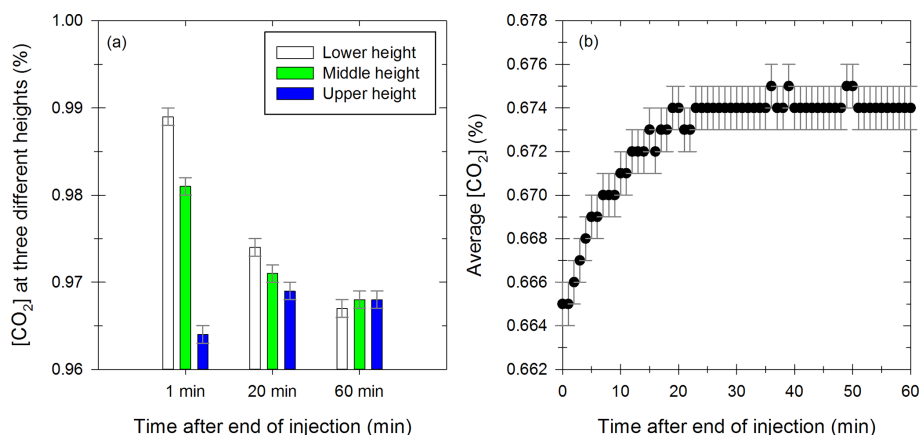
Figure 1. Determination of the mixing time in the chamber, using injection of CO_2, with measurements of the concentration at three different heights 1, 20 and 60 min after injection **(a)** and with evolution of the average concentration during 60 min after injection **(b)**.
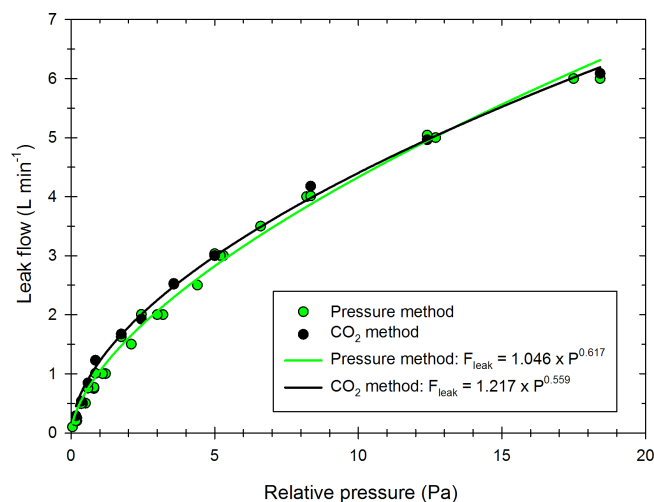

Figure 2. Values of the leak flow as a function of relative pressure, obtained with the "pressure method" (green) of the "CO_2 method" (black). The dots represent the experimental results, and the curves represent the mathematical simulation for both methods.
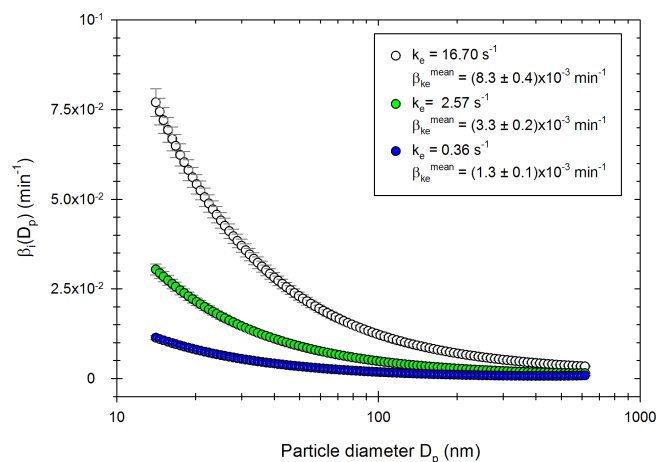
Figure 3. Distribution of the wall loss coefficient β_i (D_p) for three values of k_e obtained experimentally: $16.70\,\mathrm{s}^{-1}$ (white), $2.57\,\mathrm{s}^{-1}$ (green) and $0.36\,\mathrm{s}^{-1}$ (blue).

coefficients are very sensitive to the parameter k_e. Differences increase as the particle diameters decrease. The value of the eddy diffusivity k_e depends on the turbulence induced by the injection into the chamber and the electrostaticity of the Teflon walls, which can change between two experiments. Since experimental conditions greatly influence the turbulence and the wall deposition (Nah et al., 2017; Wang et al., 2018b), it is important to account for experiment-to-experiment variations when correcting particle losses.

In about one-third of the chamber experiments, total particle losses cannot be approximated by a simple exponential decay of [BC]. These experiments usually took place shortly after the chamber walls were manually cleaned. These actions resulted in an important electrostatic charge induced to the walls, thus increasing particle losses. For

these "charged wall" experiments, the optimized values of k_e range from 0.62 to $27.32\,\mathrm{s}^{-1}$, with an average of $7.98\,\mathrm{s}^{-1}$. These values are high but still lower than some values (36 and $269.4\,\mathrm{s}^{-1}$) found in the literature (Crump and Seinfeld, 1981; Okuyama et al., 1986). The associated values of the wall loss coefficient $\beta_{k_e}^{\mathrm{mean}}$ and the total loss coefficient $\alpha + \beta_{k_e}^{\mathrm{mean}}$ are shown in Fig. 4 with the hatched boxes for diesel (light grey) and gasoline (white). Values of $\beta_{k_e}^{\mathrm{mean}}$ are in the range $[3.82\text{–}10.67] \times 10^{-3}\,\mathrm{min}^{-1}$ for diesel and $[1.66\text{–}4.26] \times 10^{-3}\,\mathrm{min}^{-1}$ for gasoline. Respective mean values are 7.13×10^{-3} and $2.92 \times 10^{-3}\,\mathrm{min}^{-1}$. Values of $\alpha + \beta_{k_e}^{\mathrm{mean}}$ are in the range $[4.19\text{–}11.05] \times 10^{-3}\,\mathrm{min}^{-1}$ for diesel and $[2.04\text{–}5.01] \times 10^{-3}\,\mathrm{min}^{-1}$ for gasoline. Respective mean values are 7.69×10^{-3} and $3.73 \times 10^{-3}\,\mathrm{min}^{-1}$. The high values of k_e show the importance of accounting for size-dependent losses.
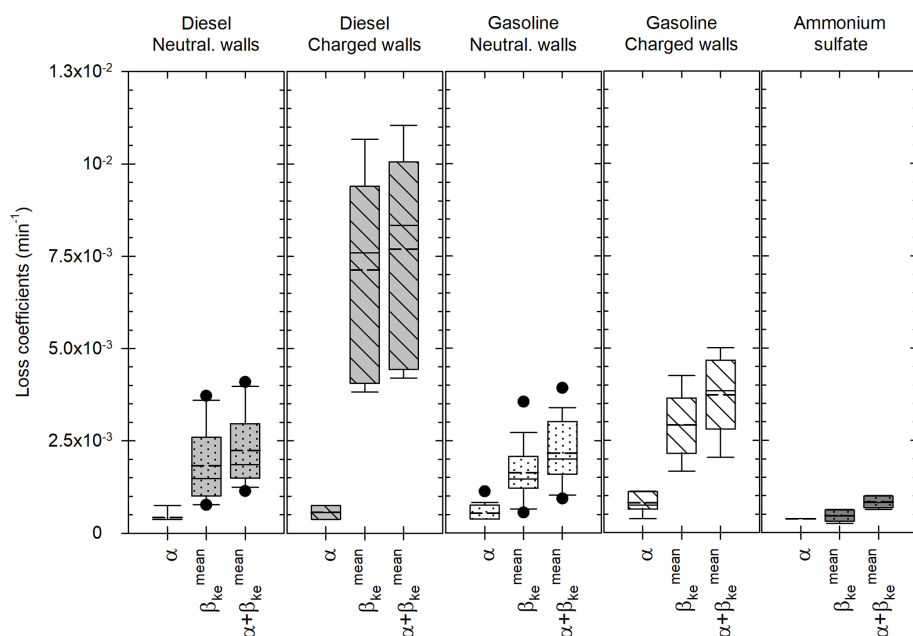
Figure 4. Leakage coefficient α, wall loss coefficient $\beta_{k_e}^{\mathrm{mean}}$ (accounting for channel size) and total loss coefficient $\alpha + \beta_{k_e}^{\mathrm{mean}}$ for the chamber experiments performed with particles from diesel (light grey) and gasoline (white) engines, as well as ammonium sulfate particles (dark grey). Coefficients for the diesel and gasoline experiments are sorted into two categories: "neutralized wall" experiments for which [BC] evolution follows a first-order exponential decay (dotted boxplots) or "charged wall" experiments for which [BC] evolution follows a second-order exponential decay (hatched boxplots). The boxes represent the 25th and 75th percentiles. The solid line in the center represents the median; the dashed line represents the mean. The whiskers are the 10th and 90th percentiles.

Also, the average agreement between [PM] corrections of step 3 (see Appendix E) is $(94.7 \pm 2.6)\,\%$.

For the remaining experiments (69 %), total particle losses are well approximated by a simple exponential decay of [BC]. Values of k_{BC} range from 1.11×10^{-3} to $3.15 \times 10^{-3}\,\mathrm{min}^{-1}$ for vehicle exhaust experiments. Values of $k_{\mathrm{PM}}^{\mathrm{amm\ sul}}$ range from 5.27×10^{-4} to $1.17 \times 10^{-3}\,\mathrm{min}^{-1}$ for ammonium sulfate experiments. For those experiments, the average agreement between [PM] corrections obtained during step 3 (according to the calculation of Appendix E) is $(97.2 \pm 2.5)\,\%$. The losses found for these experiments are lower than for the "charged wall" experiments. This is because the wall electrostatic charges have been neutralized with deposition of particles during previous experiments. The associated values of k_e for those "neutralized wall" experiments range from 0.04 to $3.23\,\mathrm{s}^{-1}$ (vehicle exhaust) and from 0.001 to $0.06\,\mathrm{s}^{-1}$ (ammonium sulfate). These values are in the range of what has been found in previous studies. Charan et al. (2018) found values of k_e between 0.015 and $8.06\,\mathrm{s}^{-1}$ in simulations of wall losses in Teflon environmental chambers. The values of the wall loss coefficient $\beta_{k_e}^{\mathrm{mean}}$ and of the total loss coefficient $\alpha + \beta_{k_e}^{\mathrm{mean}}$ associated with those "neutralized wall" experiments are shown in Fig. 4 (dotted boxes) for diesel (light grey), gasoline (white) and ammonium sulfate (dark grey). Values of $\beta_{k_e}^{\mathrm{mean}}$ are in the ranges [0.76–

3.72] $\times 10^{-3}\,\mathrm{min}^{-1}$ for diesel, [0.55–3.55] $\times 10^{-3}\,\mathrm{min}^{-1}$ for gasoline and [0.25–0.63] $\times 10^{-3}\,\mathrm{min}^{-1}$ for ammonium sulfate. Respective mean values are 1.82×10^{-3}, 1.63×10^{-3} and $0.46 \times 10^{-3}\,\mathrm{min}^{-1}$. Values of $\alpha + \beta_{k_e}^{\mathrm{mean}}$ are in the ranges [1.14–4.09] $\times 10^{-3}\,\mathrm{min}^{-1}$ for diesel, [0.93–3.93] $\times 10^{-3}\,\mathrm{min}^{-1}$ for gasoline and [0.63–1.01] $\times 10^{-3}\,\mathrm{min}^{-1}$ for ammonium sulfate. Respective mean values are 2.24×10^{-3}, 2.16×10^{-3} and $0.83 \times 10^{-3}\,\mathrm{min}^{-1}$. The mean wall loss coefficients $\beta_{k_e}^{\mathrm{mean}}$ for the "neutralized wall" experiments are 3.9 (diesel) and 1.8 (gasoline) times lower than for the "charged wall" experiments. The mean $\alpha + \beta_{k_e}^{\mathrm{mean}}$ values for the "neutralized wall" experiments are 3.4 (diesel) and 1.7 (gasoline) times lower than for the "charged wall" experiments. This is close to what was found by Wang et al. (2018a), with particle loss rates 3–4 times higher between "undisturbed" and "disturbed" experiments.

Over all the chamber experiments, the obtained values of k_e range over 4 orders of magnitude. Among those experiments, the ones with ammonium sulfate particles are those with k_e on the order of 10^{-3} to $10^{-2}\,\mathrm{s}^{-1}$. These values are low, which could be attributed to specific experimental conditions (as explained below). Moreover, the values on the order of magnitude $10^1\,\mathrm{s}^{-1}$ were all found for experiments associated with highly electrostatically charged walls (e.g., with high wall losses). It could explain the high values of k_e. Finally, without considering those specific conditions

(ammonium sulfate and highly charged wall experiments), the values of k_e range over 2 orders of magnitude. In the simulations of particle wall deposition made by Charan et al. (2018), the values of k_e used in the model also range over 2 orders of magnitude (from 0.015 to 8.06 s^{-1}). The values found under the standard conditions of this study are in a similar range (from 0.04 to 3.23 s^{-1}). The diversity of k_e values therefore seems reasonable. It could represent the easily variable wall charges induced by possible perturbations near the chamber (Wang et al., 2018b).

Figure 4 shows that the leakage coefficients α are on the same order for all conditions. They only vary from 0.38×10^{-3} to 1.13×10^{-3} min^{-1}. This is because the dilution air was injected with flows varying only between 3 and 9 L min^{-1}. Moreover, leakage coefficients are much smaller than the wall loss coefficients for the diesel and gasoline experiments. They represent 19 % and 7 % of the total loss coefficients for diesel experiments with neutralized and charged walls, respectively. For gasoline experiments, these values are 24 % and 22 %, respectively. Wall losses therefore appear to be the main contribution of total particle losses in the chamber for exhaust experiments. For ammonium sulfate experiments, total loss coefficients are smaller than for exhaust experiments. Leakage therefore represents a bigger share and accounts for 45 % of the total losses.

Figure 4 also shows that particles from diesel and gasoline engines cover a wide range of $\alpha + \beta_{k_e}^{\mathrm{mean}}$ coefficients, especially for some diesel experiments. This is mostly due to the fact that some of those experiments took place when the walls were electrostatically charged. The first experiments performed with charged walls (e.g., with the highest electrostatic charge) were with diesel engine particles. This explains the very high values reached by the diesel "charged wall" coefficients. Ammonium sulfate particles have lower loss coefficients than engine particles and remain in a narrow range. Ammonium sulfate experiments took place outside of campaigns with vehicular emissions. There were fewer perturbations near the chamber (less motion, fewer people, less heat from the instruments). Also, the flow at which they were introduced in the chamber (5.6 L m^{-1}) is much lower than for vehicle exhaust experiments (20–60 L min^{-1}). Finally, there were fewer instruments in the chamber, inducing a lower sampling flow. Since perturbations near a chamber can easily induce charges on the walls (Wang et al., 2018b), it is reasonable to assume that the specific experimental conditions of the ammonium sulfate experiments can explain the lower loss coefficients. It shows the interest of accounting for experiment-to-experiment variations. For the ammonium sulfate experiments, the total loss coefficient (leak and wall losses) found with the four-step correction method ranges from 8×10^{-6} to 2×10^{-5} s^{-1} for particles of diameter 100 nm. Nah et al. (2017) studied the wall loss coefficient ammonium sulfate of particles in a 12 m^3 chamber. They found values of β at 100 nm around $1–5 \times 10^{-5}$ s^{-1}. The values found in this study are in pretty good agreement

with what was found by Nah et al. (2017). Also, the magnitude of the corrections was computed for each cycle, using the average ratio of corrected [PM] divided by measured [PM]. For the neutralized wall experiments, corrected [PM] is on average (1.5 ± 0.4) times higher than measured [PM]. For the charged wall experiments, corrected [PM] is on average (2.8 ± 1.5) times higher than measured [PM]. For the ammonium sulfate experiments, corrected [PM] is on average (1.3 ± 0.2) times higher than measured [PM]. Moreover, Platt et al. (2013) found a particle half-life between 3.3 and 4 h. This is equivalent to having [BC] decay coefficients of 3.5×10^{-3} and 2.9×10^{-3} min^{-1}, respectively. Over a 10 h-long experiment, this would give corrected [PM] 3.4 and 2.7 times higher than measured [PM] (respectively). The corrections applied in our study therefore appear to be in a reasonable range. These elements indicate that the correction method developed in this study gives good results, consistent with what is found for other chambers of comparable size. Figure 4 shows that the experimental conditions are likely to impact the loss coefficients (as seen for the ammonium sulfate experiments). This shows the advantage of the four-step correction method, which accounts for experiment-to-experiment variations. It is not based on the assumption that the particles of the study have the same losses as those measured before or after a campaign with ammonium sulfate particles, under possibly different conditions. Figure 4 also shows that the electrostatic state of the walls appears to be the most important factor determining particle losses to the walls.

To make sure that the coefficient $\alpha + \beta_{k_e}^{\mathrm{mean}}$ accurately represents total particle losses, it is compared to k_{BC} and should be similar. To investigate this, $\alpha + \beta_{k_e}^{\mathrm{mean}}$ coefficients of "neutralized wall" experiments (e.g., for which [BC] follows a simple exponential decay giving a k_{BC} coefficient) are plotted in Fig. 5 as a function of k_{BC} or $k_{\mathrm{PM}}^{\mathrm{amm\ sul}}$.

Figure 5 shows that there is a good correlation between both loss rates $\alpha + \beta_{k_e}^{\mathrm{mean}}$ and k_{BC}. The correlation is also good for ammonium sulfate experiments, between $\alpha + \beta_{k_e}^{\mathrm{mean}}$ and $k_{\mathrm{PM}}^{\mathrm{amm\ sul}}$. The average ratio of these two coefficients for ammonium sulfate experiments is 1.04. A linear regression is performed over all the exhaust and ammonium sulfate experiments. It gives a slope of 1.08 ± 0.15. The fact that values of $\alpha + \beta_{k_e}^{\mathrm{mean}}$ are slightly higher than values of k_{BC} could be due to the size dependence of wall losses, which results in different total loss coefficients depending on the size distribution. Overall, the correlation shows that the optimized value $\alpha + \beta_{k_e}^{\mathrm{mean}}$ gives a good representation of total losses due to leakage and wall deposition. This result indicates that the complementarity of the [PM] correction using [BC] and the size-dependent correction is relevant. The coefficients $\alpha + \beta_i$ (D_p) can therefore be applied to each particle size bin, since $\alpha + \beta_{k_e}^{\mathrm{mean}}$ accurately describes the total particle losses. Results of Fig. 5 also show that loss rates of ammonium sulfate particles are generally lower than those from diesel or gaso-
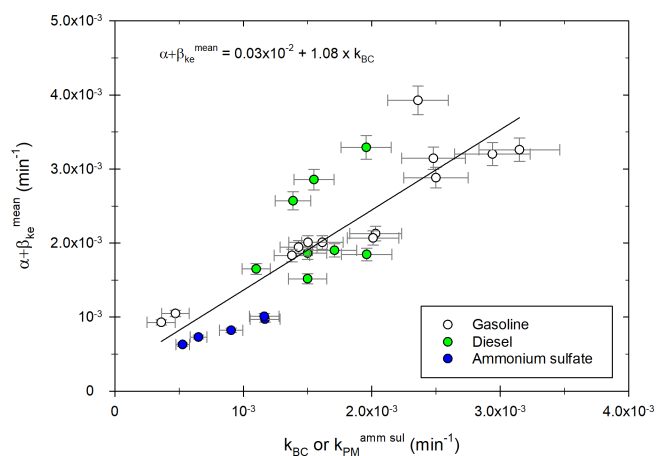
Figure 5. Mean loss coefficient $\alpha + \beta_{k_e}^{mean}$ as a function of the decay coefficient k_{BC} or $k_{PM}^{amm\ sul}$ obtained for the "neutralized wall" chamber experiments performed with particles from diesel (green) and gasoline (white) engines or ammonium sulfate particles (blue). A linear fit of the data is shown (black line).

line experiments, as found previously (Fig. 4). This can be attributed to specific experimental conditions. It shows the interest of using the four-step correction method described above, which gives corrections for each experiment without using loss rates obtained with ammonium sulfate particles before or after a campaign, under possibly different conditions.

3.2 Emission factors of particles, BC and IVOCs from diesel vehicles

Vehicle emissions are quantified in order to discuss the impact of each vehicle type and driving condition on initial chamber concentration and associated physical evolutions. Emission factors of PN, PM and BC are estimated from initial concentrations in the chamber by applying the dilution ratio. Initial concentrations are taken right after the chamber is well mixed. At that moment, no corrections for leakage or wall losses have yet been applied. This means that the concentrations taken for the computation of emission factors are those directly measured by the instruments. Moreover, as described above, some experiments occurred while the walls were highly electrostatically charged, meaning that particles can deposit onto the walls during the injection phase. This can therefore impact the initial concentrations of PN, PM and BC and thus the computed emission factors. It is difficult to estimate the associated losses. PN emission factors found in the literature for Euro 5 diesel vehicles under UC and MW conditions (Louis et al., 2016) are in the same range as those of this study. This indicates that the possible effects of wall charge are negligible. No specific correction was therefore applied to the initial concentrations. The concerned cycles are clearly identified in Fig. 6. Finally, since particle EFs

are computed from the chamber, the dilution ratio associated with their measurement is quite different from that associated with measurements directly from exhaust. Considering partitioning theory, it is important to specify the dilution ratio, especially for comparison of PM EFs with other studies. For the Euro 3 (D1), cat DPF Euro 5 (D5) and Euro 6 (D6) vehicles, the total dilution ratio in the chamber is 97 for UC and 65 for MW. For the Euro 4 (D2) vehicle, the ratio is 97 for UC and 130 for MW. For the add DPF Euro 5 (D3) vehicle, the ratio is 97 for UC and 65–130 for MW. Finally, for the add DPF Euro 5 (D4) vehicle, the ratio is 19–387 for UC and 26 for MW.

Moreover, since condensation and nucleation partly depend on the concentration of organic material, emissions of IVOCs and certain SVOCs are quantified. They are measured directly from exhaust to estimate the quantity of available organic material in the chamber. Finally, NMHC emissions are measured from the CVS to discuss the share of IVOCs which is identified. Six diesel vehicles (Euro 3 to Euro 6) are tested under both UC and MW conditions. Results are shown in Fig. 6: EFs of PN (a), PM (b), BC (c), IVOCs (d), NMHCs (e), and the ratio (%) of the IVOC EFs over the NMHC EFs.

Figure 6 shows that PM and BC EFs have a good correlation for all vehicles and driving conditions, with slightly higher emissions for PM than BC. BC accounts on average for $(62 \pm 34)\%$ of PM, which is consistent with particle composition. The Euro 3 (D1) and Euro 4 (D2) vehicles emit more PN, PM and BC than the Euro 5 (D3, D4, D5) and Euro 6 (D6) ones, with factors 10–70 000 (PN), 10–50 000 (PM) and 4–4000 (BC). Under urban conditions the Euro 5 (D3 to D5) vehicles EFs of BC, PN and PM cover a large range of values. This can be explained by the diversity and proper functioning of aftertreatment technologies for this category of vehicles (cat and add DPFs). DPFs are more effective at a certain exhaust temperature, usually not reached during a cold start urban cycle. This can lead to variations in the particle emissions. The Euro 5 vehicle with cat DPF (D5) shows PN emissions much higher under MW than under UC conditions (factor 5.7). For those cycles, the PN mode is below 19 nm, which could indicate a DPF regeneration.

IVOC and NMHC EFs are highest for the Euro 3 (D1), Euro 4 (D2) and Euro 5 with cat DPF (D5) vehicles. They are in the ranges 501–1576 µg km^{-1} and $(3–113) \times 10^3$ µg km^{-1} for IVOCs and NMHCs, respectively. IVOC emissions from the Euro 5 vehicle with cat DPF (D5) are 5.3 times and 26.8 times higher than those from the vehicles with add DPFs (the Euro 5 D3 and the Euro 6 D6, respectively). The additive and catalyzed DPFs seem to have different impacts on IVOC and NMHC emissions. Under UC conditions, the Euro 3 vehicle (D1) emits more IVOCs than the add DPF Euro 5 vehicle (D3) and the cat DPF vehicle (D5), with respective factors of 10.7 and 1.2. This is close to what was reported by Zhao et al. (2015), with a ratio 7 under creep conditions between cat DPF-equipped and non-aftertreatment ve-
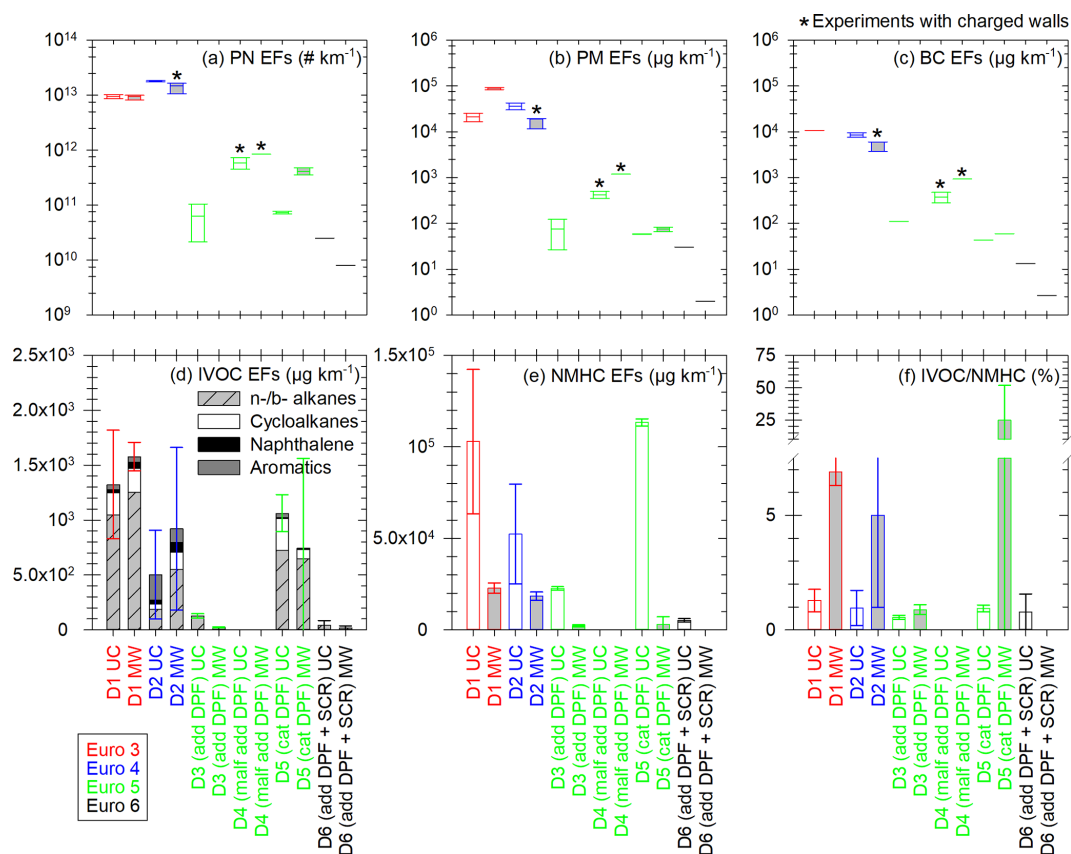
Figure 6. Emission factors of PN **(a)**, PM **(b)**, BC **(c)**, IVOCs **(d)** and NMHCs **(e)**, and IVOC / NMHC ratio **(f)** for the six tested Euro 3–6 diesel vehicles UC (white) and MW (light grey) conditions. IVOC EFs **(d)** are the sum of EFs of linear and branched (n- and b-, respectively) alkanes (hatched grey), cycloalkanes (white), naphthalene (black) and aromatics (dark grey), with retention times in the range corresponding to C_{12}–C_{22} alkanes. EFs are given in $\mu g\,km^{-1}$ and the IVOC / NMHC ratio in percentage. Vehicles are sorted by Euro norm: Euro 3 in red, Euro 4 in blue, Euro 5 with add or cat DPF in green and Euro 6 in black. The Euro 5 vehicle showing signs of malfunctioning DPF is referred to as "D4 (malf add DPF)". The boxes represent the 25th and 75th percentiles. The solid line in the center represents the median. The whiskers are the 10th and 90th percentiles. Error bars represent 1 standard variation in panels **(d)** to **(f)**. Panel **(f)** has a broken axis to better show the smaller values. The boxplots with the sign * represent the cycles for which chamber initial concentrations can be impacted by electrostatic charge on the walls. It could only impact PN, PM and BC, since IVOCs and NMHCs were sampled directly from emissions.

hicles. Moreover, the driving conditions also impact IVOC emissions. For the DPF-equipped vehicles, IVOC EFs are 1.4 to 6.2 times higher under UC conditions than under MW conditions. This is due to more complete combustion at high-temperature operations. This follows the same trend as what was reported by Zhao et al. (2015) for diesel vehicles, with ratios from 6 to 23 between creep/idle and high-speed conditions. For the Euro 3 (D1) and Euro 4 (D2) vehicles, IVOC emissions are, respectively, 1.2 and 1.8 times higher under UC conditions. This could be due to the cold start.

Moreover, for non-DPF vehicles (D1 and D2), IVOC emissions are dominated by n- and b-alkanes, which account for 64 %. Naphthalene accounts for 6 % of IVOC emissions. Cycloalkanes and aromatics account, respectively, for 14 % and 16 % of IVOC emissions. These results are consistent with those obtained by Lu et al. (2018) and Zhao et al. (2015). They found IVOC emissions of non-DPF diesel vehicles to

be dominated by cyclic compounds and alkanes (mainly unspeciated), with also a fraction of aromatics. For the cat DPF vehicle (D5), alkanes represent 78 % of IVOCs, followed by cycloalkanes (19 %) and then aromatics and naphthalene (2 % and 1 %, respectively). For the vehicles with add DPFs (D3 and D6), only alkanes are identified in the IVOC retention time range.

The IVOC / NMHC ratios range from (0.5 ± 0.1) % to (6.9 ± 0.6) % for all vehicles, except for the cat DPF Euro 5 (D5) one under MW conditions, with a ratio of (24.7 ± 27.1) %. The possible regeneration observed from PN emissions for this vehicle under MW conditions could explain high IVOC emissions and therefore a high IVOC / NMHC ratio. The average IVOC / NMHC ratio is (3.5 ± 2.9) % for the vehicles without DPF (D1 and D2) and (0.8 ± 0.2) % for the DPF-equipped vehicles (D3, D5, D6), without the possible regeneration value. This is substantially

lower than the values of $(60 \pm 10)\%$ and $(150 \pm 80)\%$ found by Zhao et al. (2015), respectively, for non-aftertreatment and DPF-equipped diesel vehicles. However, respectively, only about $(8.1 \pm 2.3)\%$ and $(5.6 \pm 3.1)\%$ of the total IVOC mass given by Zhao et al. (2015) was identified. This brings the IVOC / NMHC ratios to $(4.9 \pm 2.2)\%$ (non-aftertreatment) and $(8.4 \pm 9.1)\%$ (DPF-equipped) when considering only the identified portion of IVOCs. This is higher than what is found in this study but remains in the same range if uncertainties are accounted for.

Certain n- and b- alkanes corresponding to SVOCs are also sampled on the sorbent tubes. Their emissions are higher for the Euro 3 (D1), Euro 4 (D2) and cat DPF Euro 5 (D5) vehicles, with average EFs of 1093 and $1520\,\mu g\,km^{-1}$ under UC and MW conditions, respectively. For the Euro 5 (D3) and Euro 6 (D6) vehicles, both equipped with add DPFs, the average SVOC EFs are 263 and $247\,\mu g\,km^{-1}$ under UC and MW conditions, respectively. However, their quantification is performed with response factors from compounds with different carbon numbers (C_{20} for vehicles D1 and D5 and C_{16} for vehicles D2, D3 and D6). This can induce important uncertainties in their EFs. Also, only certain SVOCs are sampled on sorbent tubes (Lu et al., 2018). It is likely that actual emissions of SVOCs are higher than those measured here.

Considering the French fleet (André et al., 2014) and EFs of Fig. 6, the contribution of each Euro norm to particle and IVOC emissions from diesel passenger cars is estimated. Since no vehicle of norms pre-Euro, Euro 1 and Euro 2 was tested, their emissions are assumed to be in the same range as those from Euro 3 vehicles. They are grouped in a category named Euro pre-1-2-3. Figure 7a gives the French passenger car fleets from 2015 to 2030 (André et al., 2014). Figure 7b and c give the evolution of total PM and IVOC emissions, computed as the product of emission factors and fleet composition (assuming a constant number of vehicles). Figure 7d and e show the contribution of each Euro norm to total diesel passenger car emissions of PM and IVOCs.

Results show that total diesel PC emissions decrease by factors of 15.8 for PM and 7.2 for IVOCs between 2010 and 2030, assuming the total number of vehicles remains constant. This is due to evolution in the PC fleet composition, with diesel vehicles representing 58 % of the PC fleet in 2010, 65 % in 2020 and 44 % in 2030. Moreover, the share of more polluting diesel PCs (Euro pre-1-2-3 and Euro 4) evolves, representing 56 % of the fleet in 2010, 20 % in 2020 and 2 % in 2030. However, due to their much higher PM emissions (compared to Euro 5 and Euro 6 diesel vehicles), their share in total PM emissions remains dominant: almost 100 % in 2010, 99 % in 2020 and still 97 % in 2030.

For IVOCs, emissions are also due to DPF-equipped vehicles (Euro 5 and Euro 6). The share of those vehicles in IVOC emissions by diesel PCs is less than 1 % in 2010, 46 % in 2020 and 78 % in 2030. More modern vehicles will be the main contributor to IVOC emissions in 2030, with effects on particle physical and photochemical evolutions. More in-

vestigations should therefore be conducted to estimate their emissions and evolutions.

3.3 Evolution of particles from diesel exhaust

In this part, the physical processes with effects on particle number, mass and size are investigated for the six diesel vehicles (Euro 3 to Euro 6) under both UC and MW conditions. Data are corrected for leakage and wall losses using the new four-step correction method.

Figure 8a gives the hourly increase in [PM] for the vehicles classified by Euro norm. It shows that the Euro 3 and Euro 4 vehicles have the higher [PM] hourly increases. The increase in [PM] observed in this section is not likely to be an artifact induced by the correction method, as indicated by the observation of measured (e.g., uncorrected) data. This is discussed in Appendix F. Increases are at least $5\%\,h^{-1}$ during more than 500 min and up to $17\%\,h^{-1}$ during 100 min for Euro 3. The Euro 4 vehicle has hourly [PM] increases in the same range and undergoes an increase during an average of 400 min. This increase in [PM] could in part be explained by condensation of organic material onto preexisting particles (IVOCs and SVOCs). The partitioning of IVOCs and potential role in [PM] evolution are discussed in Appendix G. The emissions of IVOCs observed in Fig. 6 for the Euro 3 and Euro 4 vehicles seem to confirm this explanation. Some data on SVOCs found in the literature (Lu et al., 2018; Zhao et al., 2015) indicate that the presence of SVOCs in exhaust gas of the Euro 3 and Euro 4 vehicles is likely. It is confirmed with measurements performed in this study (Sect. 3.2). SVOCs could participate significantly in the [PM] evolution of the Euro 3 and Euro 4 vehicles due to their partitioning (Appendix G). The IVOC and SVOC emissions from the Euro 5 vehicles could explain the slight increase in particle mass during evolution presented in Fig. 8a. This increase for the Euro 5 vehicles can go up to $5\%\,h^{-1}$ during almost 5 h. The Euro 6 vehicle however, does not undergo any [PM] increase, which is consistent with the very low emissions of precursors.

The observed [PM] increase trends can be explained by different processes. First of all, condensation of organics (SVOCs and IVOCs) onto preexisting particles is the most obvious explanation. However, it is not likely to occur during several hours without the presence of a source. One hypothesis could be to consider the walls as a source. Indeed, organics deposit onto Teflon walls, and this process in known to be reversible (Matsunaga and Ziemann, 2010). In addition to being a sink for the gas phase, the walls could also represent a source of pollutants (Kaltsonoudis et al., 2019). Even though deposition is generally estimated to lower SOA formation, the impact of vapor deposition of organics onto the walls is not well described yet, and many parameters remain uncertain (Pratap et al., 2020; Yeh and Ziemann, 2015). That is, Zhang et al. (2015) observed evaporation from the walls when the temperature increases from 25 to $45\,^\circ C$. In
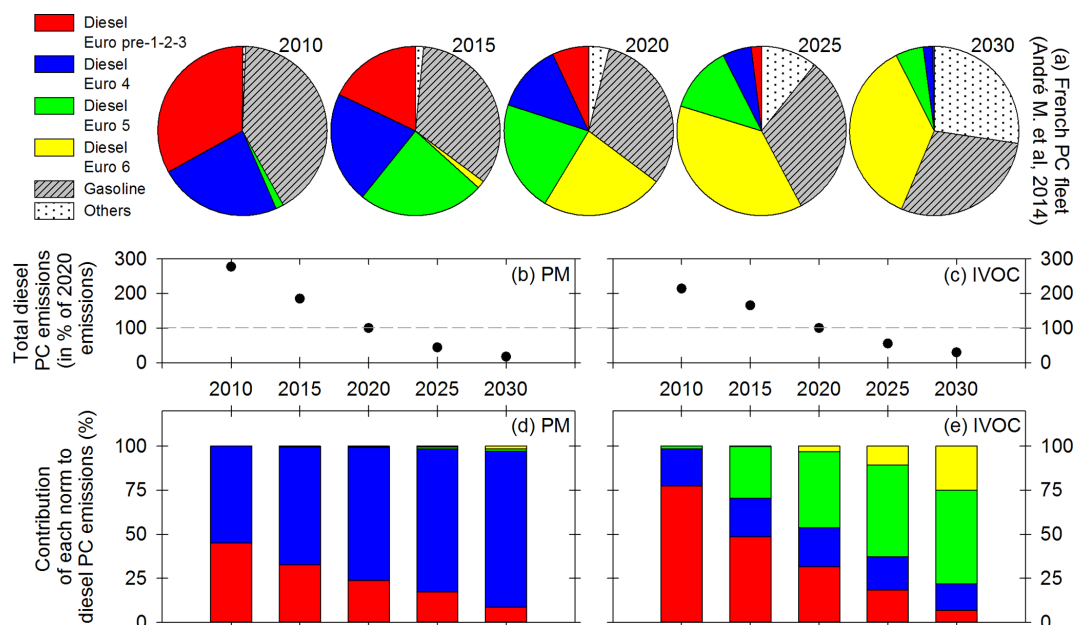
Figure 7. Evolution of the French passenger car fleet **(a)** given by André et al. (2014) for diesel vehicles of norm Euro pre-1-2-3 (red), Euro 4 (blue), Euro 5 (green) and Euro 6 (yellow) as well as gasoline vehicles (hatched grey) and vehicles with other motorizations like hybrid or electrical (dotted white). Total emissions of PM **(b)** and IVOCs **(c)** by diesel PCs given as a percentage of the 2020 emissions. Contribution of each Euro norm to diesel PC emissions of PM **(d)** and IVOCs **(e)**. Results are given for the years 2010, 2015, 2020, 2025 and 2030.
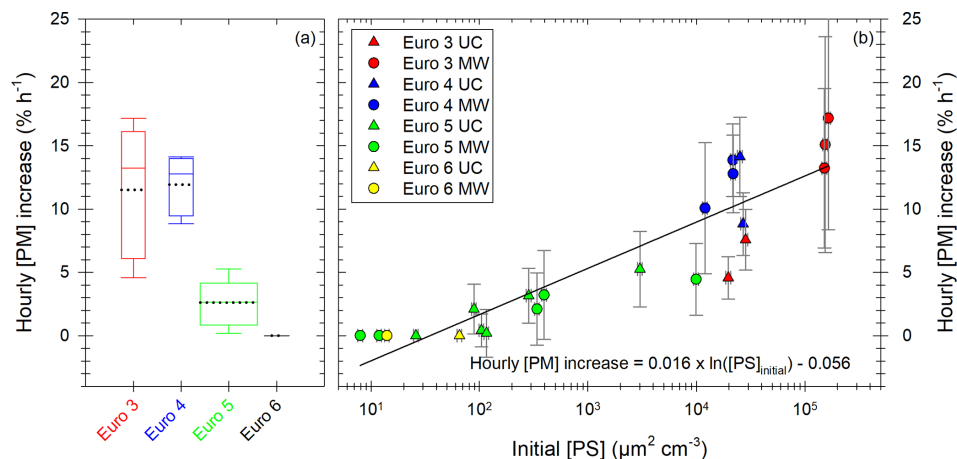
Figure 8. Particle mass hourly increase in percentage of initial [PM] per hour. Results in **(a)** are given for all the diesel vehicles sorted by Euro norm. The boxes represent the 25th and 75th percentile. The solid line in the center represents the median; the dashed line represents the mean. The whiskers are the 10th and 90th percentiles. The width of the boxes is proportional to the data set of the box. Results in **(b)** are given as a function of initial particle surface [PS] for all Euro norms (Euro 3 in red; Euro 4 in blue; Euro 5 in green; Euro 6 in yellow or black) and under both UC (triangles) and MW (circles) conditions. The x axis is presented with a logarithmic scale. A logarithmic fit of the data is performed (black line) with equation written in panel **(b)**. Error bars in panel **(b)** represent 1 standard variation.

the Euro 3 and Euro 4 experiments, the temperature increases slowly during evolution time (due to instrumentation in the laboratory) by 5 °C on average. This is a slight increase, and even though it is to this day impossible to quantify the mass of organics which could evaporate, the walls of the chamber may in some cases be a source of organic material. Moreover, vapor wall deposition is a competing process with conden-

sation onto particles. At high particle concentrations, vapor wall deposition becomes less significant (Zhang et al., 2015, 2014). This could explain why [PM] increase is higher when initial particle concentrations are high. Since for low particle concentrations the share of organics depositing onto the walls is more important, it has more impact on [PM] evolution. Overall, the walls could play the role of a source of

organic material, which might partly explain the increase in [PM] during several hours. Finally, when concentrations of organics are high enough, nucleation may occur, leading to nucleation-mode particles. If those particles are too small to be detected by the SMPS, they can grow due to coagulation or condensation and at some point be detected by the SMPS. This would result in an increase in particle number and particle mass. This phenomenon is discussed in Appendix H. It can be part of the interpretation of [PM] increase. However, considering the size of such particles and their low relative mass (compared to bigger particles), this phenomenon is not likely to be responsible for much of the total [PM] increase. Finally, the [PM] increase trends could be due to a decrease in particle density during evolution. If the decrease in density is not accounted for, it could falsely indicate an increase in [PM]. However, particle density appears to increase during particle evolution according to Peng et al. (2016). Therefore, considering a constant density (as is done in this study) could possibly minimize [PM] increase but not falsely induce it.

Figure 8b shows the [PM] hourly increase as a function of initial particle surface [PS]. A logarithmic correlation appears, indicating that conditions with high initial particle surface are more likely to lead to an increase in [PM]. The high hourly [PM] increases ($5\,\%\,h^{-1}$–$17\,\%\,h^{-1}$) are mainly due to Euro 3 and Euro 4 vehicles, whereas Euro 5 and Euro 6 vehicle experiments result in lower [PM] increases ($0\,\%\,h^{-1}$–$5\,\%\,h^{-1}$). The correlation can be explained by the fact that high initial [PS] results in a high probability of organic material finding available surface for condensation. The logarithmic shape indicates that at some point, [PM] increase is limited by other factors. This regime is reached when [PS] is above $\sim 10^4\,\mu m^2\,cm^{-3}$. A limiting factor could be the availability of organic material. Similar trends were observed by Charan et al. (2020), with initial surface areas above $\sim 1800\,\mu m^2\,cm^{-3}$ becoming insignificant for SOA yields (the numerical difference is not surprising considering the fact that the experimental protocol is quite different from that of this study). This could explain why the three points with higher initial [PS] (1 order of magnitude above the preceding ones) have an hourly [PM] increase on the same order of magnitude as the preceding points.

In addition to the hourly [PM] increase, the time during which condensation occurs is an important piece of information. Results giving the time needed to reach the maximum of PM concentration are displayed in Fig. 9a. It is plotted as a function of the initial particle surface, and the labels give the hourly [PM] increase.

Figure 9 clearly shows that when the available particle surface is high ($> 10^5\,\mu m^2\,cm^{-3}$), the time to reach the maximum [PM] is quite short and does not exceed 2.5 h. However, for initial surfaces below $4 \times 10^4\,\mu m^2\,cm^{-3}$, [PM] increase seems to be a very slow process. Even though uncertainties become large after 6 h of evolution, it seems that [PM] increase can occur slowly during 7 to 10 h. This difference between fast and slow [PM] increases is shown in Fig. 9b and

c for two examples of [PM] evolution with time. [PM] evolution is given relatively, as a percentage of [PM] max, for two experiments with low (Fig. 9b) and high (Fig. 9c) initial particle surface. The first curve (Fig. 9b) shows slow [PM] increase, with the maximum reached after 450 min. The second curve (Fig. 9c) however shows a fast evolution, with an increase occurring during 105 min. This fast [PM] increase seems to be mostly determined by the high particle surface available. By taking the average initial particle surface and the average time to reach maximum [PM] for both groups (fast and slow [PM] increases), it appears that [PM] increase is 4 times faster when the initial total particle surface is multiplied by 6.5.

Other than condensation, nucleation and coagulation are two processes that can have important effects on particle concentrations and distributions. Both of those processes are investigated, and results are shown in Fig. 10.

Figure 10a and b show the evolution of small particles (in the bins centered at 18.1 and 20.2 nm) for two experiments with respective initial [PN] of 9.1×10^3 and $2.8 \times 10^4\,cm^{-3}$. In both cases, concentrations increase during the first 30 to 60 min of the evolution. The increase in particles with such small diameters could be due to growth of smaller particles, which are initially too small to be detectable by the SMPS. Such particles could be nucleation particles formed shortly after injection. Their growth due to coagulation or condensation could explain the increase in 18–20 nm particles of Fig. 10a and b. These figures seem to indicate the presence of nucleation-mode particles formed shortly after injection. This is discussed below with results of Fig. 11.

Figure 10c and d give the evolution of the particles in three diameter bins for experiments with initial [PN] of 1.3×10^5 and $2.5 \times 10^5\,cm^{-3}$, respectively. In Fig. 10c, the particles around 18.1 nm have a constant concentration. This could mean that they coagulate and that this coagulation is compensated by the growth of smaller particles initially undetected by the SMPS. This means that there might also be nucleation-mode particles under those conditions. This is consistent with particle size distributions presented in Appendix H. It would however have limited impact on particle number evolution. A small nucleation mode under those high-concentration conditions is also consistent with the [PM] increase. Indeed, at high particle concentrations, organic material is more likely to condense rather than nucleate. Moreover, the concentrations of the particles in bin 46.1 nm decrease rapidly during 20 to 30 min. Simultaneously, the concentration of larger particles (in the bin 250.3 nm) increases. This seems to indicate that particles around 46.1 nm coagulate to form larger particles. The same trends are observed in Fig. 10d, with coagulation of larger particles (around 113.4 nm) forming particles with diameters around 385.4 nm. In both cases (Fig. 10c and d), there might be nucleation-mode particles formed at the beginning of the evolution, without a significant impact on particle number evolution. Coagulation of particles is however an important process.
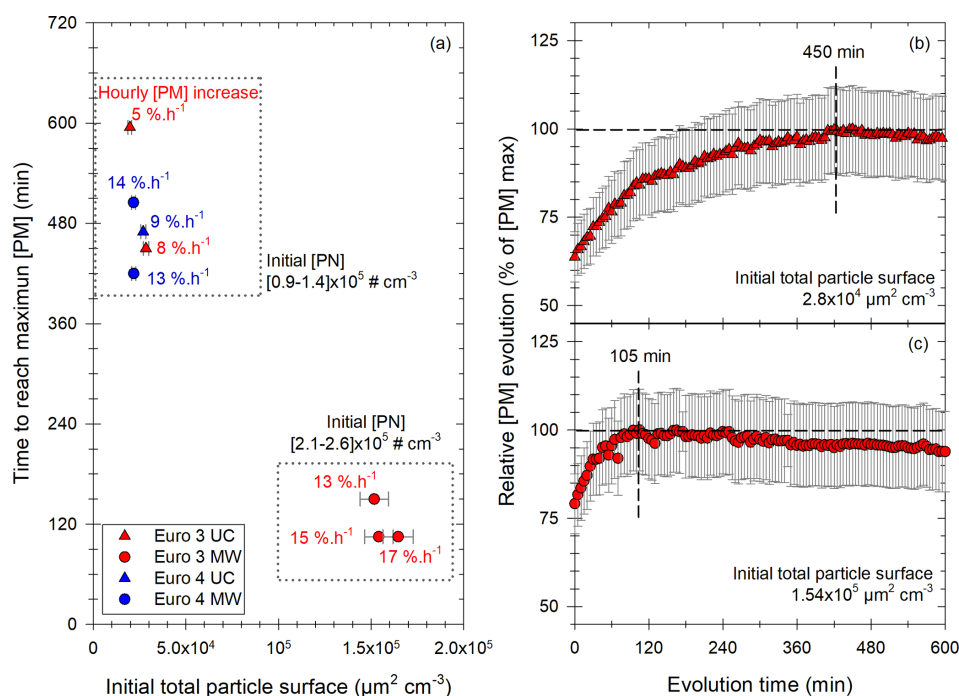
Figure 9. Results of the study of the [PM] evolution in the chamber for experiments showing a significant increase with the Euro 3 (red) and Euro 4 (blue) vehicles, under UC (triangles) or MW (circles) conditions. Panel **(a)** gives the time to reach the maximum of [PM] as a function of initial total particle surface. Each point has a label giving the hourly [PM] increase in percentage of initial [PM] per hour. Two groups are found: the first one (top) for initial [PN] between 0.9 and $1.4 \times 10^5 \, \text{cm}^{-3}$, the second one (bottom) for initial [PN] between 2.1 and $2.6 \times 10^5 \, \text{cm}^{-3}$. Panels **(b)** and **(c)** give two examples of those [PM] evolutions with time, plotted as the relative evolution of the maximum [PM]. Examples are taken: **(b)** from the first group of panel **(a)** with an initial surface of $2.8 \times 10^{-4} \, \mu\text{m}^2 \, \text{cm}^{-3}$ and a maximum [PM] reached in 450 min and **(b)** from the second group of panel **(a)** with an initial surface of $1.54 \times 10^5 \, \mu\text{m}^2 \, \text{cm}^{-3}$ and a maximum [PM] reached in 105 min.

As those two processes (coagulation of the particles in the SMPS range and growth of nucleation-mode particles) impact the total number of particles, the conditions under which they occur are investigated with regards to total [PN] evolutions. Figure 11 shows the [PN] evolution (at the beginning of the evolution) as a function of initial [PN]. It also illustrates the different profiles that [PN] evolutions can have for several initial PN concentrations.

Figure 11a shows on the x axis the relative [PN] evolution in percentage of the initial concentration per hour for different initial particle concentrations on the y axis. It shows that at low initial PN concentrations (up to $\sim 10^3 \, \text{cm}^{-3}$), [PN] evolution is not significant and is either positive or negative but remains low. Figure 11h shows an evolution with low initial concentration. [PN] remains quite steady during the 5 h of evolutions. When initial [PN] increases in the range 10^3 up to $[8\text{–}9] \times 10^4 \, \text{cm}^{-3}$, PN concentrations increase as well, up to $24 \, \% \, \text{h}^{-1}$. Figure 11e, f and g show relative [PN] evolution with initial [PN] in that range (10^3 to $[8\text{–}9] \times 10^4 \, \text{cm}^{-3}$). They show medium to high particle increase. This occurs between 90 and 120 min. This increase could be explained by the growth of nucleation-mode particles (formed at the beginning of the evolution) which are

initially not detectable by the SMPS (as mentioned above). Ning and Sioutas (2010) showed that organic vapors nucleate more easily when particle concentrations are low and condense more easily when particle concentrations are high. Imhof et al. (2006) showed that nucleation would occur more easily under low traffic density (e.g., with lower initial particle concentrations). Moreover, they found that nucleation-mode particles increase until the surface area of soot particles reaches a threshold of $0.5 \times 10^4 \, \mu\text{m}^2 \, \text{cm}^{-3}$. In this study, nucleation particles seem to be observed and significant for initial [PN] below $[8\text{–}9] \times 10^4 \, \text{cm}^{-3}$. The equivalent surface concentration is $[1.2\text{–}2] \times 10^4 \, \mu\text{m}^2 \, \text{cm}^{-3}$. This is on the same order of magnitude (factor 2–4) as the threshold found experimentally by Imhof et al. (2006). This confirms that a nucleation mode can be present under our experimental conditions. This nucleation mode would grow due to coagulation or condensation and become detectable by the SMPS. It would explain the increase in [PN] under those conditions during 90 to 120 min. Guo et al. (2020) observed growth of nucleation particles during about 2 h. This seems to confirm the interpretation of [PN] increase due to the growth of nucleation-mode particles becoming detectable by the SMPS. Therefore, the observed [PN] increase in this work
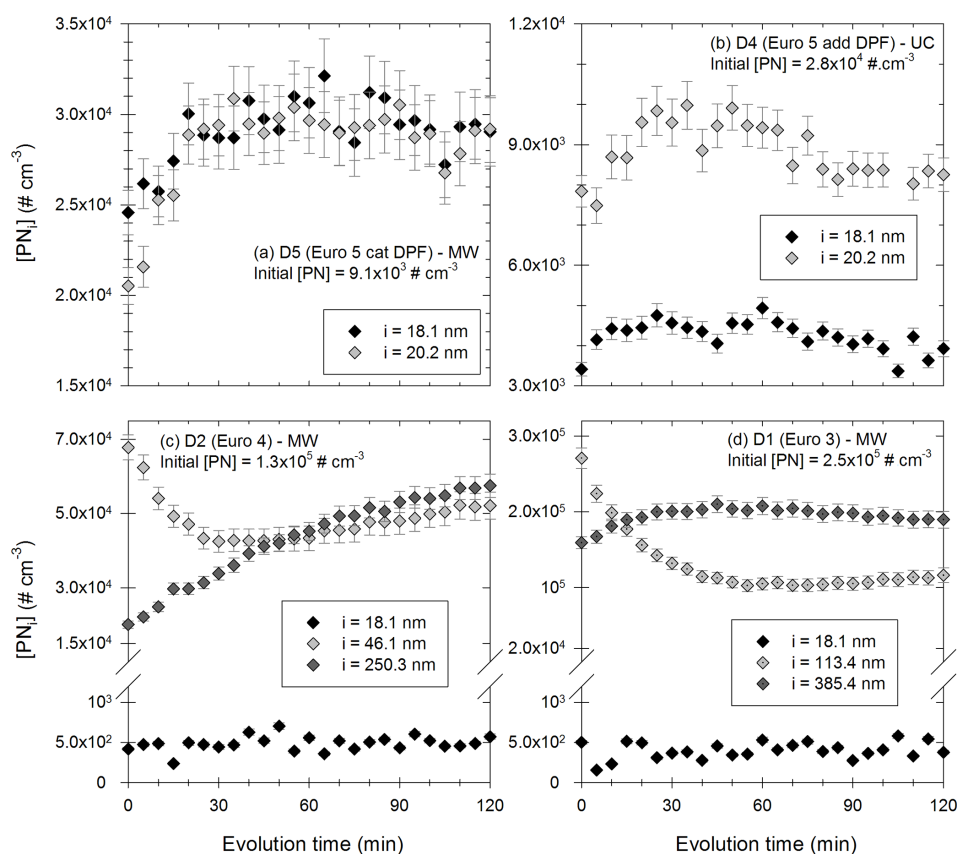
Figure 10. Evolution with time of the particles $[PN_i]$ in certain diameter bins during 2 h. Panels **(a)** and **(b)** show particles in the bins 18.1 nm (black) and 20.2 nm (light grey) for experiments with vehicle D5 under MW conditions with an initial [PN] of 9.1×10^3 cm^{-3} and with vehicle D4 under UC conditions with an initial [PN] of 2.8×10^4 cm^{-3}, respectively. Panel **(c)** shows particles in the bins 18.1 nm (black), 46.1 nm (light grey) and 250.3 nm (dark grey) with vehicle D2 under MW conditions with an initial [PN] of 1.3×10^5 cm^{-3}. Panel **(d)** shows particles in the bins 18.1 nm (black), 113.4 nm (light grey) and 385.4 nm (dark grey) with vehicle D1 under MW conditions with an initial [PN] of 2.5×10^5 cm^{-3}.

is not a physical creation of particles during several hours, since nucleation would occur rapidly after injection. Once the nucleation mode is formed, the actual trend of total particle evolution would be a decrease due to coagulation. The increase in [PN] which is observed is therefore an artifact due to the measurement range of the SMPS. This artifact is predominant for initial concentrations below $[8–9] \times 10^4$ cm^{-3}. Under those conditions, the process of coagulation cannot be quantified with this chamber and the experimental setup described in this study.

When initial particle concentration is over $[8–9] \times 10^4$ cm^{-3}, the main evolution becomes negative. It remains negative during 40 to 120 min. It can reach -27% h^{-1}, clearly showing that coagulation is occurring. Figure 11b, c and d give examples of the [PN] decrease for those high PN initial concentration conditions. Under those conditions of initial concentrations, growth of nucleation particles does not seem to be significant, as seen in Fig. 10. The evolution of [PN] is therefore mainly explained by the process of coagulation of the particles in the SMPS range.

Under those conditions, this process can be observed and quantified with this chamber and experimental setup. A slight increase can also be observed in the second half of the experiments. It could in part be explained by growth of nucleation-mode particles. As discussed for Fig. 10c and d, the nucleation mode would be relatively small under those conditions, with limited effects. It would therefore coagulate slowly, thus explaining why the increase is observed at the end of the experiments. Also, considering the error bars, which are more important when the [PN] becomes lower (e.g., when time increases), the slight increase does not seem to be significant.

Moreover, the characteristic timescale for coagulation (time necessary for reduction of initial [PN] by a factor of 2) was computed using Eq. (13.67) from Seinfeld and Pandis (2016), assuming monodisperse distributions and considering initial particle concentration. For the experiments with initial concentrations below $[8–9] \times 10^4$ cm^{-3}, the range of characteristic timescales indicates that the time needed to reach 50 % of the initial concentration is between 11 and
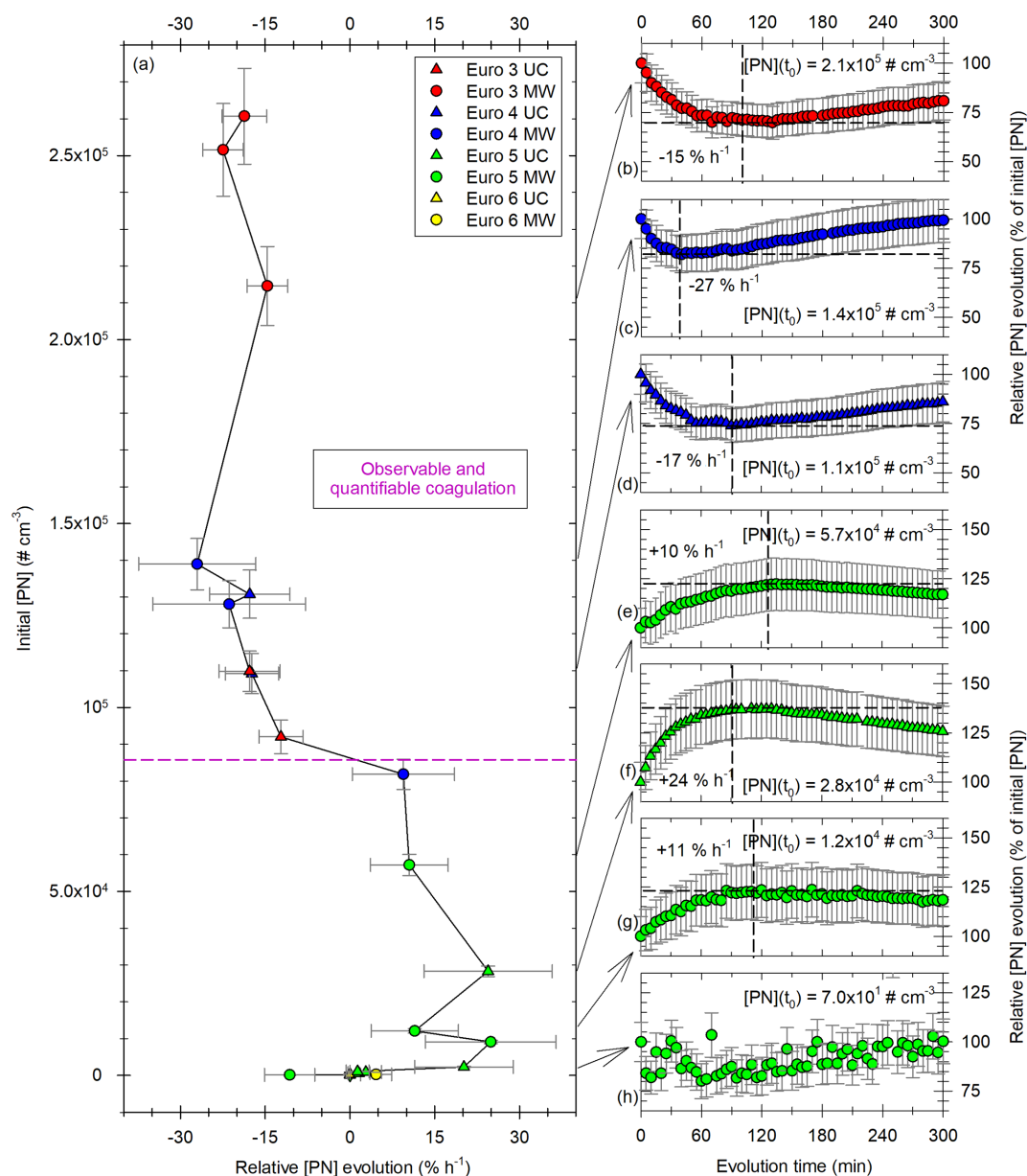
Figure 11. Evolutions of total [PN] for the vehicles of all Euro norms (Euro 3 in red; Euro 4 in blue; Euro 5 in green; Euro 6 in yellow) and in both UC (triangles) and MW (circles) driving. Panel **(a)** on the y axis is the initial particle concentration, plotted versus the [PN] evolution, expressed in percentage of the initial concentration per hour. The horizontal pink dashed line shows the concentration above which it is estimated that coagulation becomes observable and quantifiable with this chamber. Panels **(b)** to **(h)** show examples of such [PN] evolutions with time, expressed relatively as a percentage of initial [PN], for several initial concentrations ranging between 7.0×10^1 and 2.1×10^5 cm^{-3}. The vertical dashed lines indicate the time at which the [PN] evolution stops or changes, with the percentage of initial [PN] reached at this time shown by the horizontal dashed line and with the average hourly evolution during this period.

40 000 h. This could explain why coagulation is not observed for low initial concentrations in Fig. 11a. For the experiments with initial concentrations above $[8–9] \times 10^4$ cm^{-3}, the characteristic timescale ranges between 3.4 and 9.7 h. This means that significant [PN] decrease due to coagulation can occur in a few hours. It confirms that coagulation is observable under our experimental conditions with high initial concentrations,

as shown in Fig. 11a. Coagulation therefore seems to be more significant for initial concentrations above $[8–9] \times 10^4$ cm^{-3}. With the chamber and experimental setup of this study, coagulation is observable and quantifiable only for initial concentrations above this value.

4 Conclusion

This study presents the characterization of a new $8\,\mathrm{m^3}$ environmental chamber with Teflon walls meant to study the physical evolution of primary pollutants emitted by road traffic. A new size-dependent method to correct particle losses due to leakage and wall deposition was developed and applied. It accounts for experiment-to-experiment variations. It consists of four steps using the [BC] decay and wall loss coefficients from the theory of Crump and Seinfeld (1981). These two complementary parts are in good agreement. The total loss coefficients $\alpha + \beta_{k_e}^{\mathrm{mean}}$ of "charged wall" experiments are in the range $[4.19–11.05] \times 10^{-3}\,\mathrm{min^{-1}}$ for diesel and $[2.04–5.01] \times 10^{-3}\,\mathrm{min^{-1}}$ for gasoline. For "neutral wall" experiments, they are in the range $[1.25–4.09] \times 10^{-3}\,\mathrm{min^{-1}}$ for diesel, $[0.93–3.93] \times 10^{-3}\,\mathrm{min^{-1}}$ for gasoline and $[0.63–1.01] \times 10^{-3}\,\mathrm{min^{-1}}$ for ammonium sulfate. The wall charges appear to be the most important factor affecting particle wall losses. They are responsible for 76 % to 93 % of total losses for exhaust experiments and for 55 % in the case of ammonium sulfate experiments. Results of wall losses obtained from ammonium sulfate particle experiments show similar trends to those found in the literature for a chamber of comparable size.

EFs of PN, PM, BC and IVOCs for Euro 3 to Euro 6 diesel vehicles were studied in detail in order to understand their role in particle evolution under dark conditions. For non-DPF vehicles (D1 and D2), IVOC emissions are dominated by n- and b-alkanes (64 %), followed by cycloalkanes (14 %) and aromatics (16 %). For the cat DPF vehicle (D5), alkanes represent 78 % of IVOCs, followed by cycloalkanes (19 %) and then aromatics (2 %). For the vehicles with add DPFs (D3 and D6), only alkanes were identified in the IVOCs.

Moreover, this study presents results of evolution in the dark of particles emitted by diesel passenger cars. It is shown that [PM] increase can reach 17 % h^{-1} without the effects of photochemistry. Uncorrected measurements confirm that this is not an artifact induced by the correction method. It could in part be explained by the walls playing the role of source of organic material. [PM] increase appears to have a logarithmic correlation with initial [PS]. The [PM] increase in older diesel vehicles (Euro 3 and Euro 4) is enhanced in comparison to modern vehicles. This is due to their higher emissions of BC, PN and PM compared to DPF-equipped vehicles as well as their emissions of IVOCs and SVOCs. In several cases with high initial [PM], a fraction of IVOCs (0.8 % to 34.0 %) and SVOCs (85.5 % to 99.9 %) can be found in the particle phase and participate in the physical evolution of particles. The increase in [PM] is also found to be 4 times faster when the available surface is multiplied by 6.5. However, when initial [PS] is above $\sim 10^4\,\mathrm{\mu m^2\,cm^{-3}}$, [PM] increase seems to be limited. The quantity of organic material available could be a limiting factor. Finally, this study shows that nucleation-mode particles are likely to be present for initial concentrations below $[8–9] \times 10^4\,\mathrm{cm^{-3}}$. The growth of those particles results in an increase in measured [PN]. This is an artifact of the experimental setup, due to the measurement range of the SMPS, and not an actual creation of particles during several hours. This artifact prevents the study of the process of coagulation in this chamber when initial concentrations are below $[8–9] \times 10^4\,\mathrm{cm^{-3}}$. However, above this value, coagulation is the dominant process for [PN] evolutions. It leads to [PN] decrease up to $-27\,\%\,\mathrm{h^{-1}}$. Under those conditions, this chamber and this experimental setup are well suited for the observation and quantification of the coagulation process.

Results found in this study under laboratory conditions are in good agreement with tunnel observations described in the literature. They can help better understand the conditions under which physical processes are more likely to occur. They can be applied to several conditions in the dark, such as winter rush hours or tunnel evolutions.

Appendix A

Below are shown the speed profiles of the Artemis Urban and Artemis Motorway cycles.
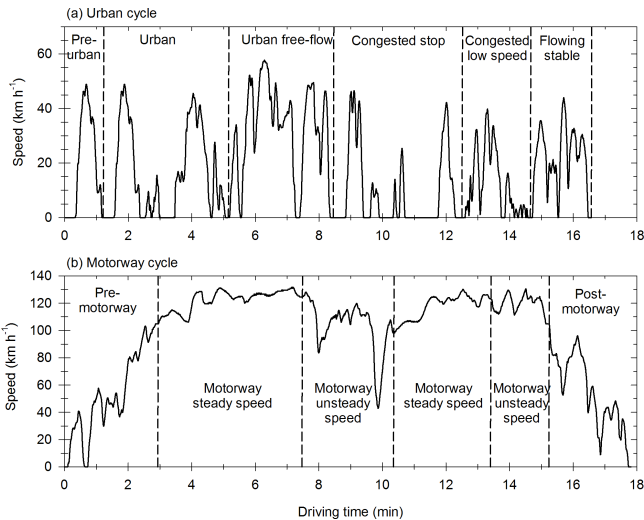

Figure A1. Speed in $km\,h^{-1}$ during the Artemis Urban cycle **(a)** and the Artemis Motorway cycle **(b)**, with the different types of driving found under those conditions.

Appendix B

Below are listed the constants taken for the calculation of $\beta(D_p)$.

- $k_B = 1.381 \times 10^{-23}\,J\,K^{-1}$ the Boltzmann constant
- T (K) the temperature in the chamber for each experiment
- $\mu = 1.8 \times 10^{-5}\,kg\,m^{-1}\,s^{-1}$ the viscosity of air
- $\rho_p = 1.2\,g\,cm^{-3}$ the particle density
- $g = 9.81\,m\,s^{-2}$ the g force
- $\lambda = 6.51\,nm$ the mean-free path of air

Appendix C

Table C1. Emission factors in $mg\,km^{-1}$ of linear (n-) and branched (b-) alkanes with carbon numbers below between 12 and 22 (C_{12}–C_{22}) and of naphthalene, cycloalkanes and aromatics measured with the ATD-GC-MS method. The sum of those EFs gives the IVOC EFs. Emission factors of n- and b-alkanes with carbon number above 22. Emission factors of NMHCs measured by flame ionization detection. Emissions below the quantification limit are indicated as "$< QL$". Ratio of IVOC / NMHC expressed as percentage of NMHCs. Results are shown for vehicles D1 (Euro 3), D2 (Euro 4), D3 (Euro 5 add DPF), D5 (Euro 5 cat DPF) and D6 (Euro 6 add DPF and SCR) under both UC and MW conditions.

Vehicle	D1		D2		D3 (add DPF)		D5 (cat DPF)		D6 (add DPF and SCR)	
Cycle	UC	MW	UC	MW	UC	MW	UC	MW	UC	MW
n-/b- alkanes C_{12}–C_{22} (mg km^{-1})	1.05±0.31	1.25±0.08	0.19±0.03	0.55±0.48	0.12±0.02	0.02±0.01	0.72±0.10	0.65±0.68	0.04±0.04	0.02±0.02
Naphthalene (mg km^{-1})	0.03±0.03	0.06±0.02	0.04±0.01	0.09±0.05	<QL	<QL	0.01±0.01	<QL	<QL	<QL
Cycloalkanes (mg km^{-1})	0.2±0.10	0.22±0.01	0.05±0.04	0.16±0.16	<QL	<QL	0.29±0.06	0.08±0.12	<QL	<QL
Aromatics (mg km^{-1})	0.04±0.49	0.05±0.13	0.23±0.40	0.12±0.74	<QL	<QL	0.04±0.17	0.01±0.82	<QL	<QL
IVOCs (mg km^{-1})	1.32±0.93	1.58±0.24	0.5±0.48	0.92±1.42	0.12±0.04	0.02±0.01	1.06±0.34	0.74±1.62	0.04±0.08	0.02±0.04
n-/b-alkanes $C_{>22}$ (mg km^{-1})	1.56±1.26	1.27±1.35	0.26±0.30	0.66±0.01	0.35±0.06	0.29±0.43	1.46±1.47	2.63±3.17	0.17±0.12	0.2±0.24
NMHCs (mg km^{-1})	102.93±39.43	22.82±2.79	52.31±27.29	18.38±2.29	22.68±0.89	2.25±0.53	113.37±2.00	3.01±4.14	5.18±0.96	No data
IVOC / NMHC (%)	1.28±0.48	6.91±0.59	0.96±0.77	5.00±4.02	0.54±0.09	0.88±0.21	0.93±0.15	24.73±27.10	0.79±0.78	No data

* QL: quantification limit.

Appendix D

Figure D1a and b show two examples of [BC] evolutions and decay fits. Figure D1a is an example of an evolution well fitted by a first-order exponential decay. Figure D1b shows an evolution not well fitted by a first-order exponential decay. For instance, the fitted initial concentration is $12.1\,\mu\text{g}\,\text{m}^{-3}$, whereas the actual initial concentration is $23.2\,\mu\text{g}\,\text{m}^{-3}$. This means that this fit would induce an error of 48 % on the initial concentration. However, the second-order exponential decay matches very well the measured values.

Appendix E

To verify how well [PM] corrections from steps 1 and 2 agree, the average relative agreement between $[\text{PM}]_{\text{corrected}}^{\text{step 1}}(t)$ and $[\text{PM}]_{\text{corrected}}^{\text{step 1}}(t)$ is computed as given in Eq. (E1).

$$\text{Agreement}(\%) = 100$$
$$-\frac{1}{n} \times \left(\sum_{i=0}^{n} \frac{\left| [\text{PM}]_{\text{corrected}}^{\text{step 1}}(t_i) - [\text{PM}]_{\text{corrected}}^{\text{step 2}}(t_i) \right|}{[\text{PM}]_{\text{corrected}}^{\text{step 1}}(t_i)} \right)$$
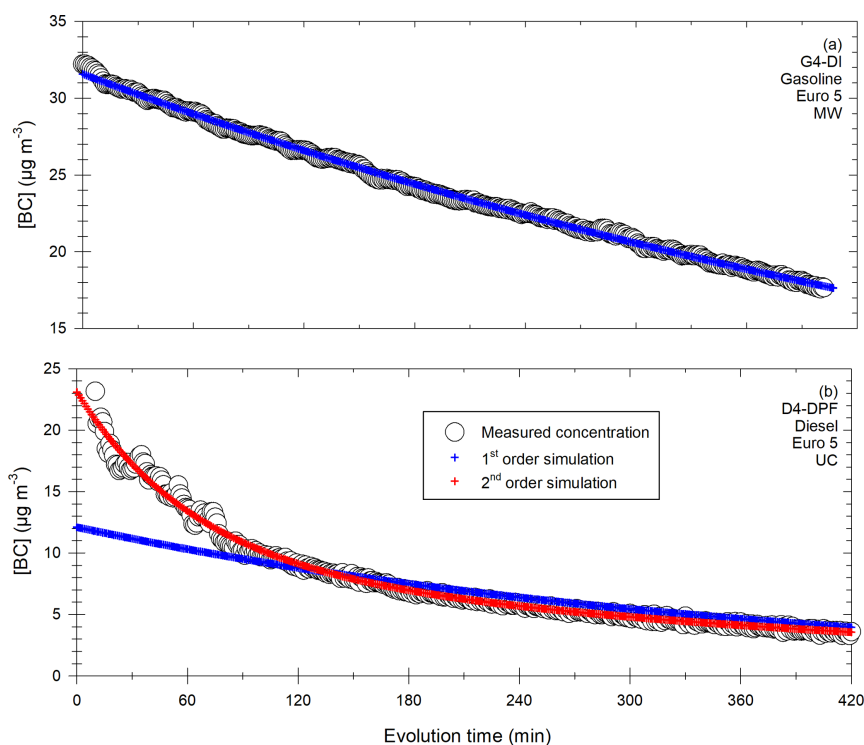$$\times 100 \tag{E1}$$

Figure D1. Evolution of the measured BC concentration (white circles) for the G4-DI vehicle under MW conditions **(a)** and the D4-DPF vehicle under UC conditions **(b)**. The curve is fitted with a first-order exponential decay (blue) in both cases and with a second-order exponential decay (red) in panel **(b)**.

Appendix F

Figure F1 shows uncorrected [PM] measurements (black crosses) and corrected [PM] for the Euro 3 (red) and Euro 4 (blue) vehicles under UC (triangles) and MW (circles) conditions. Figure F1a, b and c show "long" evolutions for which corrected [PM] reaches its maximum after several hours (> 400 min). Those figures correspond to the points on the upper left-hand side of Fig. 9a, with lower initial particle surface. Figure F1d shows a "rapid" [PM] evolution for which the corrected concentration reaches its maximum in tan 105 min. It corresponds to one of the points on the lower right-hand side of Fig. 9a, with a higher initial particle surface. For the "long" evolution of Fig. F1a, the measured concentration increases during 80 min. After that, it slightly decreases, with a decrease rate smaller than that of BC (hence the continuous increase in corrected [PM]). Figure F1b and c show that measured [PM] steadily increases during 295 to 320 min. It then remains pretty constant. Considering the fact that all of these measured concentrations (Fig. F1a to c) are subject to leakage and wall deposition, the fact that they increase during up to 6 h and then mostly remain constant shows that continuous increase in [PM] is possible during several hours. Therefore, the continuous increases in corrected [PM] observed in Figs. 8 and 9 are not likely to be an artifact induced by the correction algorithm. These increases are obviously more important and longer on corrected concentrations, but this is normal as leakage and wall deposition, which both lower [PM], are corrected. Moreover, the "rapid" evolution of Fig. F1d lasts 80 min for measured [PM], with an increase rate of 12 % h^{-1}. These values indicate that there is indeed a rapid and significant increase in [PM] during the beginning of the evolution. Then, concentrations start slowly decreasing before reaching a steady decrease rate (similarly to that of BC). This is consistent with the evolution of the corrected concentration, which increases significantly and then increases more slightly before it reaches a maximum and remains constant. Here again, it seems that the significant and rapid increase observed for corrected [PM] of Fig. F1d is not an artifact induced by the correction method.

Appendix G

The effective saturation concentrations of n-alkanes up to C_{32} are obtained with the method described in Lu et al. (2018) for VOCs ($C_{>12}$), IVOCs (C_{12}–C_{22}) and SVOCs (C_{23}–C_{32}). Using Eq. (14.43) from Seinfeld and Pandis (2016), the fraction in particle phase is computed for two conditions of initial [PM] typical of significant [PM] increase observed in Fig. 9 (200 and 2500 µg m^{-3}). The organic aerosol concentration [OA] is estimated to range roughly between 2 % and 80 % of [PM]. This range is based on studies giving the ratio [PM] / [OA] or the ratio EC/OC, which cover a wide range of values (Kostenidou et al., 2021; May et al.,
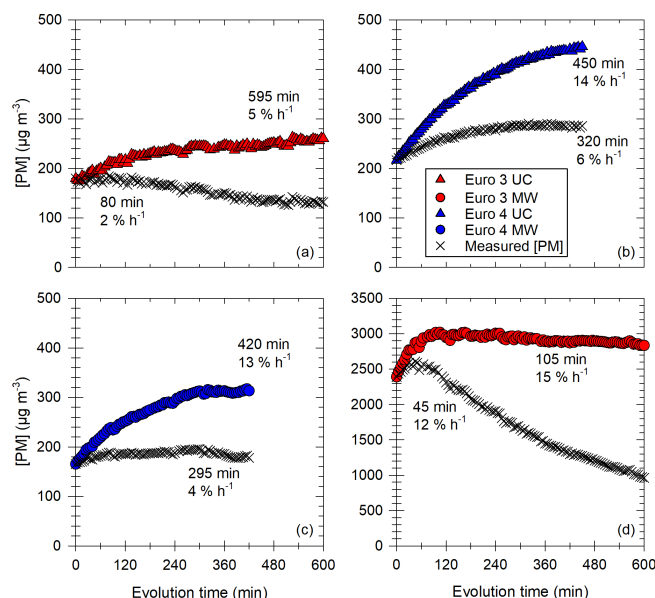

Figure F1. Evolution of the corrected PM concentrations for the Euro 3 vehicle (red) and Euro 4 vehicle (blue) under both UC (triangles) and MW (circles) conditions. Panels **(a)**, **(b)** and **(c)** represent long increases, whereas panel **(d)** represents a short increase. The corrected concentrations are compared to the measured (e.g., uncorrected) PM concentrations (black crosses). Labels give for each evolution (measured or corrected) the time at which [PM] reaches its maximum as well as the associated hourly increase.

2014). The wide range is caused by several parameters, such as measurement technique, experimental conditions, driving conditions, and vehicle type (motorization and aftertreatment technologies). Results are given in Fig. G1 as areas delimited by the lower (2 %) and upper (80 %) estimates of [PM] / [OA]. The grey area is for initial [PM] = 200 µg m^{-3} (with [OA] ranging from 4 to 160 µg m^{-3}), and the hatched blue area is for initial [PM] = 2500 µg m^{-3} (with [OA] ranging from 50 to 160 µg m^{-3}). Also, in this study, the Euro 3 and Euro 4 vehicles have differences between initial concentrations of PM and BC of about 69.6 % of initial [PM]. This indicates that [OA] could represent up to 69 % of [PM]. This value is used for another estimation of [OA]. The associated fractions are shown in Fig. G1 for initial [PM] = 200 µg m^{-3} (grey line, associated [OA] = 138 µg m^{-3}) and for initial [PM] = 2500 µg m^{-3} (dashed blue line, associated [OA] = 1725 µg m^{-3}).

For the condition with initial [PM] = 200 µg m^{-3}, the percentage of n-alkanes IVOCs present in the particle phase ranges from 0.8 % to 13.7 % for [OA] estimated as 2 % and 80 % of [PM], respectively. The percentage of n-alkanes SVOCs in the particle phase ranges from 85.5 % to 98.7 %, respectively. For the estimation with [OA] = 69 % of [PM], 12.7 % of n-alkanes IVOCs and 98.5 % of n-alkanes SVOCs are in the particle phase.
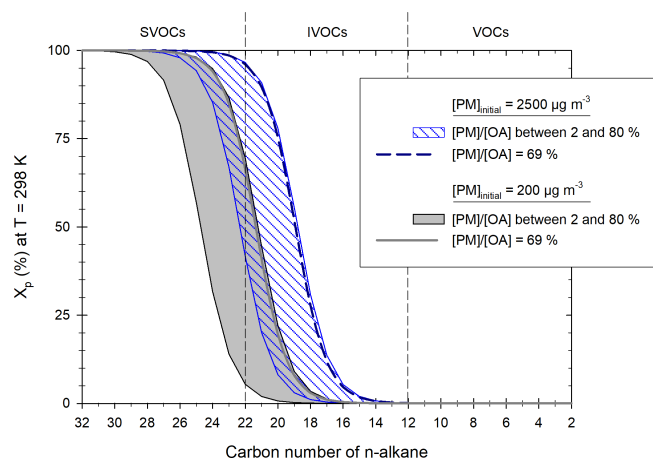
Figure G1. Particle fraction at $T = 298\,\mathrm{K}$ of n-alkanes (VOCs, IVOCs and SVOCs), in percentage, with carbon number between 2 and 32. The repartition is given assuming two initial PM concentrations of $200\,\mathrm{\mu g\,m^{-3}}$ (grey) and $2500\,\mathrm{\mu g\,m^{-3}}$ (blue), typical of significant [PM] increase. X_p is computed with different estimates of organic aerosol concentrations [OA], ranging from 2 % to 80 % of initial [PM] (grey area and blue hatched area, respectively). It is also computed assuming that [OA] = 69 % of initial [PM], with initial [PM] of $200\,\mathrm{\mu g\,m^{-3}}$ (continuous grey line) and $2500\,\mathrm{\mu g\,m^{-3}}$ (dashed blue line).

For the condition with initial [PM] = $2500\,\mathrm{\mu g\,m^{-3}}$, the percentage of n-alkanes IVOCs present in the particle phase ranges from 6.7 % to 34.0 % for [OA] estimated as 2 % and 80 % of [PM], respectively. The percentage of n-alkanes SVOCs in the particle phase ranges from 96.5 % to 99.9 %, respectively. For the estimation with [OA] = 69 % of [PM], 32.7 % of n-alkanes IVOCs and 99.9 % of n-alkanes SVOCs are in the particle phase.

These results show that at such high particle concentrations, significant fractions of n-alkanes IVOCs and n-alkanes SVOCs could be present in the particle phase. Overall, it indicates that IVOCs can participate in the [PM] evolutions observed in Figs. 8 and 9, due to high PM concentrations and the presence of IVOCs (Fig. 6d) for the Euro 3 and Euro 4 vehicles. SVOCs can also be a significant contributor to [PM] evolutions.

Appendix H

Figure H1 shows measured lognormal [PN] evolutions (e.g., not corrected) for two cycles concerned by continuous [PM] increase during several hours, as seen in Fig. 9. The cycles are from the two concerned vehicles: Euro 3 UC (Fig. H1a and b) and Euro 4 MW (Fig. H1c and d) conditions. On the left are presented the measured [PN] evolutions over the whole SMPS measurement range. On the right are presented the same data but with a focus on smaller diameters (up to 50 nm) and with a more adapted scale. It shows that under both conditions there is the presence of small particles (below 20 nm). Their concentrations show a slight decrease over the course of the experiments, but they are present until the end. They could come from growth (due to coagulation or condensation) of nucleation-mode particles. Their concentrations remaining quite constant could be because they are at the same time increasing (from growth of nucleation-mode particles) and decreasing (from their own coagulation). This phenomenon could partly explain the continuous [PM] increase observed in Figs. 8 and 9 for the Euro 3 and Euro 4 vehicles.
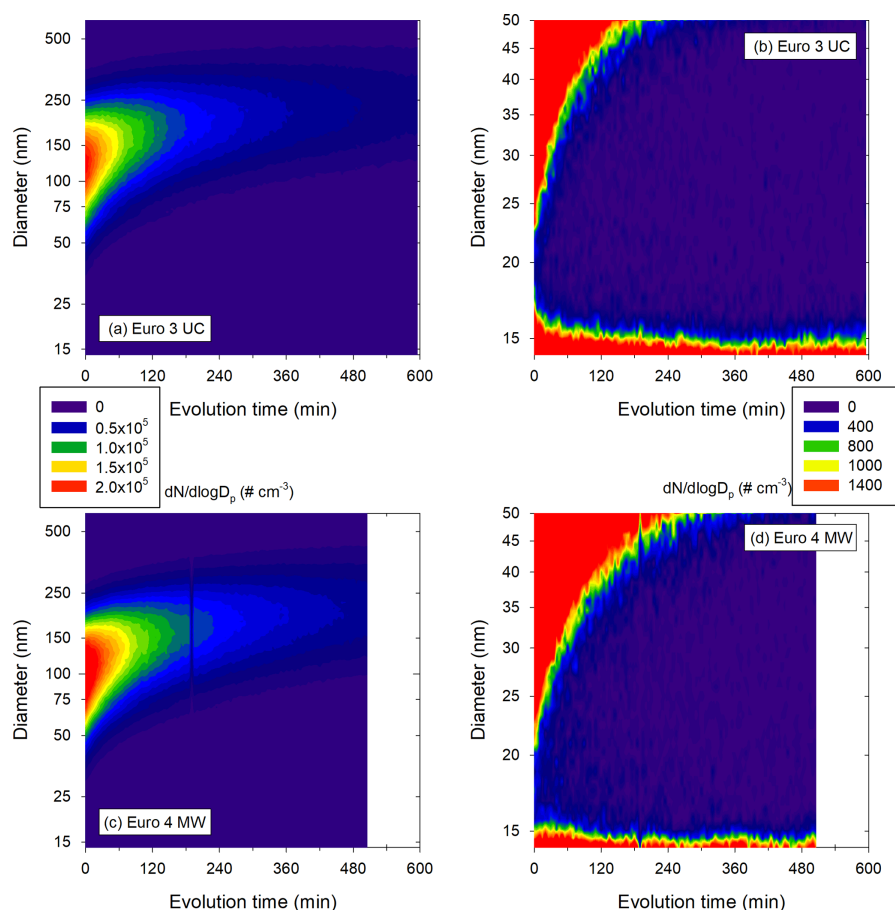
Figure H1. Measured PN distribution evolutions for the Euro 3 UC **(a, b)** and Euro 4 MW **(c, d)** conditions. The *x* axis gives the evolution time in minutes. The *y* axis gives the diameter in nanometers. The color scale gives the lognormal concentration. Panels **(a)** and **(c)** give the PN distributions for the whole SMPS measurement range. Panels **(b)** and **(d)** show the same cycles for the range 14 to 50 nm. The color scales are changed to see the smallest particles.

Data availability. All data from this study are available from the authors upon request.

Author contributions. YL, BD'A, CF, KS, CL and BV designed the research. YL, CL and BV performed and analyzed the characterization experiments. YL and BV performed and analyzed the emission and evolution experiments. CF, LF and BV performed the ATD-GC-MS analysis. EK, BTR and BD'A contributed to the experimental setup and the experimental procedure. PT and PP drove the cars and helped with the experimental setup. BV synthesized all the data and wrote the paper with contributions from CL, VC, BD'A, EK, BTR, KS, CF and YL.

Competing interests. The contact author has declared that neither they nor their co-authors have any competing interests.

Disclaimer. Publisher's note: Copernicus Publications remains neutral with regard to jurisdictional claims in published maps and institutional affiliations.

Review statement. This paper was edited by Pierre Herckes and reviewed by three anonymous referees.

References

André, M.: The ARTEMIS European driving cycles for measuring car pollutant emissions, Sci. Total Environ., 334–335, 73–84, https://doi.org/10.1016/j.scitotenv.2004.04.070, 2004.

André, M., Roche, A.-L., and Bourcier, L.: Statistiques de parcs et trafic pour le calcul des émissions de polluants des transports routiers en France, IFSTTAR, Marne-la-Vallée, France, 2014.

Andreae, M. O. and Gelencsér, A.: Black carbon or brown carbon? The nature of light-absorbing carbonaceous aerosols, Atmos. Chem. Phys., 6, 3131–3148, https://doi.org/10.5194/acp-6-3131-2006, 2006.

Babar, Z. B., Park, J.-H., Kang, J., and Lim, H.-J.: Characterization of a Smog Chamber for Studying Formation and Physicochemical Properties of Secondary Organic Aerosol, Aerosol Air Qual. Res., 16, 3102–3113, https://doi.org/10.4209/aaqr.2015.10.0580, 2017.

Barone, T. L., Lall, A. A., Storey, J. M. E., Mulholland, G. W., Prikhodko, V. Y., Frankland, J. H., Parks, J. E., and Zachariah, M. R.: Size-Resolved Density Measurements of Particle Emissions from an Advanced Combustion Diesel Engine: Effect of Aggregate Morphology, Energ. Fuel., 25, 1978–1988, https://doi.org/10.1021/ef200084k, 2011.

Charan, S. M., Kong, W., Flagan, R. C., and Seinfeld, J. H.: Effect of particle charge on aerosol dynamics in Teflon environmental chambers, Aerosol Sci. Tech., 52, 854–871, https://doi.org/10.1080/02786826.2018.1474167, 2018.

Charan, S. M., Buenconsejo, R. S., and Seinfeld, J. H.: Secondary organic aerosol yields from the oxidation of benzyl alcohol, Atmos. Chem. Phys., 20, 13167–13190, https://doi.org/10.5194/acp-20-13167-2020, 2020.

Chen, T., Liu, Y., Chu, B., Liu, C., Liu, J., Ge, Y., Ma, Q., Ma, J., and He, H.: Differences of the oxidation process and secondary organic aerosol formation at low and high precursor concentrations, J. Environ. Sci., 79, 256–263, https://doi.org/10.1016/j.jes.2018.11.011, 2019.

Chu, B., Liu, Y., Ma, Q., Ma, J., He, H., Wang, G., Cheng, S., and Wang, X.: Distinct potential aerosol masses under different scenarios of transport at a suburban site of Beijing, J. Environ. Sci., 39, 52–61, https://doi.org/10.1016/j.jes.2015.11.003, 2016.

Corner, J. and Pendlebury, E. D.: The Coagulation and Deposition of a Stirred Aerosol, P. Phys. Soc. Lond. B, 64, 645–654, https://doi.org/10.1088/0370-1301/64/8/304, 1951.

Crump, J. G. and Seinfeld, J. H.: Turbulent deposition and gravitational sedimentation of an aerosol in a vessel of arbitrary shape, J. Aerosol Sci., 12, 405–415, https://doi.org/10.1016/0021-8502(81)90036-7, 1981.

Crump, J. G., Flagan, R. C., and Seinfeld, J. H.: Particle Wall Loss Rates in Vessels, Aerosol Sci. Tech., 2, 303–309, https://doi.org/10.1080/02786828308958636, 1982.

Drozd, G. T., Zhao, Y., Saliba, G., Frodin, B., Maddox, C., Oliver Chang, M.-C., Maldonado, H., Sardar, S., Weber, R. J., Robinson, A. L., and Goldstein, A. H.: Detailed Speciation of Intermediate Volatility and Semivolatile Organic Compound Emissions from Gasoline Vehicles: Effects of Cold-Starts and Implications for Secondary Organic Aerosol Formation, Environ. Sci. Technol., 53, 1706–1714, https://doi.org/10.1021/acs.est.8b05600, 2019.

European Environment Agency: Average age of road vehicles per country, available at: https://www.eea.europa.eu/data-and-maps/daviz/average-age-of-road-vehicles-6#tab-chart_1, last access: 6 November 2020.

Giechaskiel, B., Ntziachristos, L., Samaras, Z., Scheer, V., Casati, R., and Vogt, R.: Formation potential of vehicle exhaust nucleation mode particles on-road and in the laboratory, Atmos. Environ., 39, 3191–3198, https://doi.org/10.1016/j.atmosenv.2005.02.019, 2005.

Grieshop, A. P., Logue, J. M., Donahue, N. M., and Robinson, A. L.: Laboratory investigation of photochemical oxidation of organic aerosol from wood fires 1: measurement and simulation of organic aerosol evolution, Atmos. Chem. Phys., 9, 1263–1277, https://doi.org/10.5194/acp-9-1263-2009, 2009.

Guo, S., Hu, M., Peng, J., Wu, Z., Zamora, M. L., Shang, D., Du, Z., Zheng, J., Fang, X., Tang, R., Wu, Y., Zeng, L., Shuai, S., Zhang, W., Wang, Y., Ji, Y., Li, Y., Zhang, A. L., Wang, W., Zhang, F., Zhao, J., Gong, X., Wang, C., Molina, M. J., and Zhang, R.: Remarkable nucleation and growth of ultrafine particles from vehicular exhaust, P. Natl. Acad. Sci. USA, 117, 3427–3432, https://doi.org/10.1073/pnas.1916366117, 2020.

Harrison, R. M., Rob MacKenzie, A., Xu, H., Alam, M. S., Nikolova, I., Zhong, J., Singh, A., Zeraati-Rezaei, S., Stark, C., Beddows, D. C. S., Liang, Z., Xu, R., and Cai, X.: Diesel exhaust nanoparticles and their behaviour in the atmosphere, Proc. R. Soc. A, 474, 20180492, https://doi.org/10.1098/rspa.2018.0492, 2018.

Hennigan, C. J., Miracolo, M. A., Engelhart, G. J., May, A. A., Presto, A. A., Lee, T., Sullivan, A. P., McMeeking, G. R., Coe, H., Wold, C. E., Hao, W.-M., Gilman, J. B., Kuster, W. C., de Gouw, J., Schichtel, B. A., Collett Jr., J. L., Kreidenweis, S. M., and Robinson, A. L.: Chemical and physical transformations of organic aerosol from the photo-oxidation of open biomass burning emissions in an environmental chamber, Atmos. Chem. Phys., 11, 7669–7686, https://doi.org/10.5194/acp-11-7669-2011, 2011.

Huang, R.-J., Zhang, Y., Bozzetti, C., Ho, K.-F., Cao, J.-J., Han, Y., Daellenbach, K. R., Slowik, J. G., Platt, S. M., Canonaco, F., Zotter, P., Wolf, R., Pieber, S. M., Bruns, E. A., Crippa, M., Ciarelli, G., Piazzalunga, A., Schwikowski, M., Abbaszade, G., Schnelle-Kreis, J., Zimmermann, R., An, Z., Szidat, S., Baltensperger, U., Haddad, I. E., and Prévôt, A. S. H.: High secondary aerosol contribution to particulate pollution during haze events in China, Nature, 514, 218–222, https://doi.org/10.1038/nature13774, 2014.

IARC: Outdoor aur pollution, IARC, Lyon, France, 2016.

Imhof, D., Weingartner, E., Prévôt, A. S. H., Ordóñez, C., Kurtenbach, R., Wiesen, P., Rodler, J., Sturm, P., McCrae, I., Ekström, M., and Baltensperger, U.: Aerosol and NO_x emission factors and submicron particle number size distributions in two road tunnels with different traffic regimes, Atmos. Chem. Phys., 6, 2215–2230, https://doi.org/10.5194/acp-6-2215-2006, 2006.

Jeong, C.-H., Evans, G. J., Healy, R. M., Jadidian, P., Wentzell, J., Liggio, J., and Brook, J. R.: Rapid physical and chemical transformation of traffic-related atmospheric particles near a highway, Atmos. Pollut. Res., 6, 662–672, https://doi.org/10.5094/APR.2015.075, 2015.

Kaltsonoudis, C., Jorga, S. D., Louvaris, E., Florou, K., and Pandis, S. N.: A portable dual-smog-chamber system for atmospheric aerosol field studies, Atmos. Meas. Tech., 12, 2733–2743, https://doi.org/10.5194/amt-12-2733-2019, 2019.

Kostenidou, E., Martinez-Valiente, A., R'Mili, B., Marques, B., Temime-Roussel, B., Durand, A., André, M., Liu, Y., Louis, C., Vansevenant, B., Ferry, D., Laffon, C., Parent, P., and D'Anna, B.: Technical note: Emission factors, chemical composition, and morphology of particles emitted from Euro 5 diesel and gasoline light-duty vehicles during transient cycles, Atmos. Chem. Phys., 21, 4779–4796, https://doi.org/10.5194/acp-21-4779-2021, 2021.

Kozawa, K. H., Winer, A. M., and Fruin, S. A.: Ultrafine particle size distributions near freeways: Effects of differing wind directions on exposure, Atmos. Environ., 63, 250–260, https://doi.org/10.1016/j.atmosenv.2012.09.045, 2012.

La, Y. S., Camredon, M., Ziemann, P. J., Valorso, R., Matsunaga, A., Lannuque, V., Lee-Taylor, J., Hodzic, A., Madronich, S., and Aumont, B.: Impact of chamber wall loss of gaseous organic compounds on secondary organic aerosol formation: explicit modeling of SOA formation from alkane and alkene oxidation, Atmos. Chem. Phys., 16, 1417–1431, https://doi.org/10.5194/acp-16-1417-2016, 2016.

Lambe, A. T., Onasch, T. B., Massoli, P., Croasdale, D. R., Wright, J. P., Ahern, A. T., Williams, L. R., Worsnop, D. R., Brune, W. H., and Davidovits, P.: Laboratory studies of the chemical composition and cloud condensation nuclei (CCN) activity of secondary organic aerosol (SOA) and oxidized primary organic aerosol (OPOA), Atmos. Chem. Phys., 11, 8913–8928, https://doi.org/10.5194/acp-11-8913-2011, 2011.

Leskinen, A., Yli-Pirilä, P., Kuuspalo, K., Sippula, O., Jalava, P., Hirvonen, M.-R., Jokiniemi, J., Virtanen, A., Komppula, M., and Lehtinen, K. E. J.: Characterization and testing of a new environmental chamber, Atmos. Meas. Tech., 8, 2267–2278, https://doi.org/10.5194/amt-8-2267-2015, 2015.

Louis, C., Liu, Y., Tassel, P., Perret, P., Chaumond, A., and André, M.: PAH, BTEX, carbonyl compound, black-carbon, NO_2 and ultrafine particle dynamometer bench emissions for Euro 4 and Euro 5 diesel and gasoline passenger cars, Atmos. Environ., 141, 80–95, https://doi.org/10.1016/j.atmosenv.2016.06.055, 2016.

Louis, C., Liu, Y., Martinet, S., D'Anna, B., Valiente, A. M., Boreave, A., R'Mili, B., Tassel, P., Perret, P., and André, M.: Dilution effects on ultrafine particle emissions from Euro 5 and Euro 6 diesel and gasoline vehicles, Atmos. Environ., 169, 80–88, https://doi.org/10.1016/j.atmosenv.2017.09.007, 2017.

Lu, J., Ge, X., Liu, Y., Chen, Y., Xie, X., Ou, Y., Ye, Z., and Chen, M.: Significant secondary organic aerosol production from aqueous-phase processing of two intermediate volatility organic compounds, Atmos. Environ., 211, 63–68, https://doi.org/10.1016/j.atmosenv.2019.05.014, 2019.

Lu, Q., Zhao, Y., and Robinson, A. L.: Comprehensive organic emission profiles for gasoline, diesel, and gas-turbine engines including intermediate and semi-volatile organic compound emissions, Atmos. Chem. Phys., 18, 17637–17654, https://doi.org/10.5194/acp-18-17637-2018, 2018.

Matsunaga, A. and Ziemann, P. J.: Gas-Wall Partitioning of Organic Compounds in a Teflon Film Chamber and Potential Effects on Reaction Product and Aerosol Yield Measurements, Aerosol Sci. Tech., 44, 881–892, https://doi.org/10.1080/02786826.2010.501044, 2010.

May, A. A., Nguyen, N. T., Presto, A. A., Gordon, T. D., Lipsky, E. M., Karve, M., Gutierrez, A., Robertson, W. H., Zhang, M., Brandow, C., Chang, O., Chen, S., Cicero-Fernandez, P., Dinkins, L., Fuentes, M., Huang, S.-M., Ling, R., Long, J., Maddox, C., Massetti, J., McCauley, E., Miguel, A., Na, K., Ong, R., Pang, Y., Rieger, P., Sax, T., Truong, T., Vo, T., Chattopadhyay, S., Maldonado, H., Maricq, M. M., and Robinson, A. L.: Gas- and particle-phase primary emissions from in-use, on-road gasoline and diesel vehicles, Atmos. Environ., 88, 247–260, https://doi.org/10.1016/j.atmosenv.2014.01.046, 2014.

Morawska, L., Ristovski, Z., Jayaratne, E. R., Keogh, D. U., and Ling, X.: Ambient nano and ultrafine particles from motor vehicle emissions: Characteristics, ambient processing and implications on human exposure, Atmos. Environ., 42, 8113–8138, https://doi.org/10.1016/j.atmosenv.2008.07.050, 2008.

Nah, T., McVay, R. C., Pierce, J. R., Seinfeld, J. H., and Ng, N. L.: Constraining uncertainties in particle-wall deposition correction during SOA formation in chamber experiments, Atmos. Chem. Phys., 17, 2297–2310, https://doi.org/10.5194/acp-17-2297-2017, 2017.

Ning, Z. and Sioutas, C.: Atmospheric Processes Influencing Aerosols Generated by Combustion and the Inference of Their Impact on Public Exposure: A Review, Aerosol Air Qual. Res., 10, 43–58, https://doi.org/10.4209/aaqr.2009.05.0036, 2010.

Nomura, Y., Hopke, P. K., Fitzgerald, B., and Mesbah, B.: Deposition of Particles in a Chamber as a Function of Ventilation Rate, Aerosol Sci. Tech., 27, 62–72, https://doi.org/10.1080/02786829708965458, 1997.

Okuyama, K., Kousaka, Y., Yamamoto, S., and Hosokawa, T.: Particle loss of aerosols with particle diameters between 6 and 2000 nm in stirred tank, J. Colloid Interf. Sci., 110, 214–223, https://doi.org/10.1016/0021-9797(86)90370-X, 1986.

Papapostolou, V., Lawrence, J. E., Diaz, E. A., Wolfson, J. M., Ferguson, S. T., Long, M. S., Godleski, J. J., and Koutrakis, P.: Laboratory evaluation of a prototype photochemical chamber designed to investigate the health effects of fresh and aged vehicular exhaust emissions, Inhal. Toxicol., 23, 495–505, https://doi.org/10.3109/08958378.2011.587034, 2011.

Pathak, R. K., Stanier, C. O., Donahue, N. M., and Pandis, S. N.: Ozonolysis of α-pinene at atmospherically relevant concentrations: Temperature dependence of aerosol mass fractions (yields), J. Geophys. Res., 112, D03201, https://doi.org/10.1029/2006JD007436, 2007.

Peng, J., Hu, M., Guo, S., Du, Z., Zheng, J., Shang, D., Levy Zamora, M., Zeng, L., Shao, M., Wu, Y.-S., Zheng, J., Wang, Y., Glen, C. R., Collins, D. R., Molina, M. J., and Zhang, R.: Markedly enhanced absorption and direct radiative forcing of black carbon under polluted urban environments, P. Natl. Acad. Sci. USA, 113, 4266–4271, https://doi.org/10.1073/pnas.1602310113, 2016.

Pierce, J. R., Engelhart, G. J., Hildebrandt, L., Weitkamp, E. A., Pathak, R. K., Donahue, N. M., Robinson, A. L., Adams, P. J., and Pandis, S. N.: Constraining Particle Evolution from Wall Losses, Coagulation, and Condensation-Evaporation in Smog-Chamber Experiments: Optimal Estimation Based on Size Distribution Measurements, Aerosol Sci. Tech., 42, 1001–1015, https://doi.org/10.1080/02786820802389251, 2008.

Platt, S. M., El Haddad, I., Zardini, A. A., Clairotte, M., Astorga, C., Wolf, R., Slowik, J. G., Temime-Roussel, B., Marchand, N., Ježek, I., Drinovec, L., Močnik, G., Möhler, O., Richter, R., Barmet, P., Bianchi, F., Baltensperger, U., and Prévôt, A. S. H.: Secondary organic aerosol formation from gasoline vehicle

emissions in a new mobile environmental reaction chamber, Atmos. Chem. Phys., 13, 9141–9158, https://doi.org/10.5194/acp-13-9141-2013, 2013.

Pratap, V., Kiran, S. A., Bian, Q., Pierce, J. R., Hopke, P. K., and Nakao, S.: Observation of Vapor Wall Deposition in a Smog Chamber Using Size Evolution of Pure Organic Particles, Aerosol Air Qual. Res., 20, 2705–2714, https://doi.org/10.4209/aaqr.2020.05.0268, 2020.

Rivas, I., Beddows, D. C. S., Amato, F., Green, D. C., Järvi, L., Hueglin, C., Reche, C., Timonen, H., Fuller, G. W., Niemi, J. V., Pérez, N., Aurela, M., Hopke, P. K., Alastuey, A., Kulmala, M., Harrison, R. M., Querol, X., and Kelly, F. J.: Source apportionment of particle number size distribution in urban background and traffic stations in four European cities, Environ. Int., 135, 105345, https://doi.org/10.1016/j.envint.2019.105345, 2020.

Sartelet, K., Zhu, S., Moukhtar, S., André, M., André, J. M., Gros, V., Favez, O., Brasseur, A., and Redaelli, M.: Emission of intermediate, semi and low volatile organic compounds from traffic and their impact on secondary organic aerosol concentrations over Greater Paris, Atmos. Environ., 180, 126–137, https://doi.org/10.1016/j.atmosenv.2018.02.031, 2018.

Sbai, S. E., Li, C., Boreave, A., Charbonnel, N., Perrier, S., Vernoux, P., Bentayeb, F., George, C., and Gil, S.: Atmospheric photochemistry and secondary aerosol formation of urban air in Lyon, France, J. Environ. Sci., 99, 311–323, https://doi.org/10.1016/j.jes.2020.06.037, 2020.

Schnell, M., Cheung, C. S., and Leung, C. W.: Investigation on the coagulation and deposition of combustion particles in an enclosed chamber with and without stirring, J. Aerosol Sci., 37, 1581–1595, https://doi.org/10.1016/j.jaerosci.2006.06.001, 2006.

Seinfeld, J. H. and Pandis, S. N.: Atmospheric chemistry and physics: from air pollution to climate change, 3rd edn., John Wiley & Sons, Inc., Hoboken, New Jersey, USA, 2016.

Totton, T. S., Chakrabarti, D., Misquitta, A. J., Sander, M., Wales, D. J., and Kraft, M.: Modelling the internal structure of nascent soot particles, Combust. Flame, 157, 909–914, https://doi.org/10.1016/j.combustflame.2009.11.013, 2010.

TSI: Aerosol Instrument Manager Software for Scanning Mobility Particle Sizer (SMPS) Spectrometer User's Manual, TSI Incorporated, Shoreview, MN, USA, 2010.

Verheggen, B. and Mozurkewich, M.: An inverse modeling procedure to determine particle growth and nucleation rates from measured aerosol size distributions, Atmos. Chem. Phys., 6, 2927–2942, https://doi.org/10.5194/acp-6-2927-2006, 2006.

Wang, N., Kostenidou, E., Donahue, N. M., and Pandis, S. N.: Multi-generation chemical aging of α-pinene ozonolysis products by reactions with OH, Atmos. Chem. Phys., 18, 3589–3601, https://doi.org/10.5194/acp-18-3589-2018, 2018a.

Wang, N., Jorga, S. D., Pierce, J. R., Donahue, N. M., and Pandis, S. N.: Particle wall-loss correction methods in smog chamber experiments, Atmos. Meas. Tech., 11, 6577–6588, https://doi.org/10.5194/amt-11-6577-2018, 2018b.

Wang, X., Liu, T., Bernard, F., Ding, X., Wen, S., Zhang, Y., Zhang, Z., He, Q., Lü, S., Chen, J., Saunders, S., and Yu, J.: Design and characterization of a smog chamber for studying gas-phase chemical mechanisms and aerosol formation, Atmos. Meas. Tech., 7, 301–313, https://doi.org/10.5194/amt-7-301-2014, 2014.

Weitkamp, E. A., Sage, A. M., Pierce, J. R., Donahue, N. M., and Robinson, A. L.: Organic Aerosol Formation from Photochemical Oxidation of Diesel Exhaust in a Smog Chamber, Environ. Sci. Technol., 41, 6969–6975, https://doi.org/10.1021/es070193r, 2007.

Xu, R., Alam, M. S., Stark, C., and Harrison, R. M.: Behaviour of traffic emitted semi-volatile and intermediate volatility organic compounds within the urban atmosphere, Sci. Total Environ., 720, 137470, https://doi.org/10.1016/j.scitotenv.2020.137470, 2020.

Yeh, G. K. and Ziemann, P. J.: Gas-Wall Partitioning of Oxygenated Organic Compounds: Measurements, Structure–Activity Relationships, and Correlation with Gas Chromatographic Retention Factor, Aerosol Sci. Tech., 49, 727–738, https://doi.org/10.1080/02786826.2015.1068427, 2015.

Zhang, K. M. and Wexler, A. S.: Evolution of particle number distribution near roadways – Part I: analysis of aerosol dynamics and its implications for engine emission measurement, Atmos. Environ., 38, 6643–6653, https://doi.org/10.1016/j.atmosenv.2004.06.043, 2004.

Zhang, K. M., Wexler, A. S., Zhu, Y. F., Hinds, W. C., and Sioutas, C.: Evolution of particle number distribution near roadways. Part II: the "Road-to-Ambient" process, Atmos. Environ., 38, 6655–6665, https://doi.org/10.1016/j.atmosenv.2004.06.044, 2004.

Zhang, X., Cappa, C. D., Jathar, S. H., McVay, R. C., Ensberg, J. J., Kleeman, M. J., and Seinfeld, J. H.: Influence of vapor wall loss in laboratory chambers on yields of secondary organic aerosol, P. Natl. Acad. Sci. USA, 111, 5802–5807, https://doi.org/10.1073/pnas.1404727111, 2014.

Zhang, X., Schwantes, R. H., McVay, R. C., Lignell, H., Coggon, M. M., Flagan, R. C., and Seinfeld, J. H.: Vapor wall deposition in Teflon chambers, Atmos. Chem. Phys., 15, 4197–4214, https://doi.org/10.5194/acp-15-4197-2015, 2015.

Zhao, Y., Nguyen, N. T., Presto, A. A., Hennigan, C. J., May, A. A., and Robinson, A. L.: Intermediate Volatility Organic Compound Emissions from On-Road Diesel Vehicles: Chemical Composition, Emission Factors, and Estimated Secondary Organic Aerosol Production, Environ. Sci. Technol., 49, 11516–11526, https://doi.org/10.1021/acs.est.5b02841, 2015.

Zhao, Y., Nguyen, N. T., Presto, A. A., Hennigan, C. J., May, A. A., and Robinson, A. L.: Intermediate Volatility Organic Compound Emissions from On-Road Gasoline Vehicles and Small Off-Road Gasoline Engines, Environ. Sci. Technol., 50, 4554–4563, https://doi.org/10.1021/acs.est.5b06247, 2016.

Zhao, Y., Lambe, A. T., Saleh, R., Saliba, G., and Robinson, A. L.: Secondary Organic Aerosol Production from Gasoline Vehicle Exhaust: Effects of Engine Technology, Cold Start, and Emission Certification Standard, Environ. Sci. Technol., 52, 1253–1261, https://doi.org/10.1021/acs.est.7b05045, 2018.

Zhu, J., Penner, J. E., Lin, G., Zhou, C., Xu, L., and Zhuang, B.: Mechanism of SOA formation determines magnitude of radiative effects, P. Natl. Acad. Sci. USA, 114, 12685–12690, https://doi.org/10.1073/pnas.1712273114, 2017.